Precambrian Research 272 (2016) 78–100

Contents lists available at ScienceDirect

Precambrian Research

journal homepage: www.elsevier.com/locate/precamres

Sedimentation, metamorphism and granite generation in a back-arc region: Records from the Ediacaran Nova Venécia Complex (Araçuaí Orogen, Southeastern Brazil)

Fabiana Richter[a,*], Cristiano Lana[a], Gary Stevens[b], Ian Buick[b], Antônio Carlos Pedrosa-Soares[c], Fernando Flecha Alkmim[a], Kathryn Cutts[a]

[a] Applied Isotope Research Group, Universidade Federal de Ouro Preto, Ouro Preto, Brazil
[b] Department of Earth Sciences, Stellenbosch University, Stellenbosch, South Africa
[c] Instituto de Geociencias, Universidade Federal de Minas Gerais, Belo Horizonte, Brazil

ARTICLE INFO

Article history:
Received 24 July 2015
Received in revised form 3 October 2015
Accepted 17 October 2015
Available online 28 October 2015

Keywords:
Nova Venecia
Araçuai
Orogen
Granulite
Braziliano

ABSTRACT

The Nova Venécia migmatite-granulite-granite Complex (NVC) in the core of the Araçuaí Orogen (AO, 630–480 Ma), southeast Brazil, exposes a mid-crustal section with abundant evidence for high-grade metamorphism linked to production, extraction and emplacement of peraluminous melts. Although the AO represents the textbook example of a confined orogen, there is surprisingly a lack of detailed studies on its metamorphic evolution related to widespread granitogenesis occurring from the Neoproterozoic to early Paleozoic. In this study, we combine U–Pb geochronology and metamorphic petrology to constrain the evolution of the NVC migmatitic metasedimentary granulites, from deposition to high-grade metamorphism, and to correlate the metamorphic history of the terrain with the several episodes of granite magmatism (G1–G5) in the AO. The sedimentation of the NVC can be bracketed within a maximum 13 My period, between its maximum depositional age at ca. 606 Ma and the intrusion of early syn-collisional granitoids at 593 Ma. Compilation of available U–Pb data shows that the bulk of the magmatic rocks in the AO (G1 + G2 rocks) crystallized contemporaneously over a period of 15 My (ca. 595–570 Ma) with a peak at ca. 575 Ma. Although it is inferred a protracted period of crustal heating in the AO (from ca. 640–480), U–Pb ages of metamorphic and magmatic zircons and monazites suggest at least two major heat pulses at ca. 593–560 and 523–495 Ma. The timing of peak regional metamorphism is constrained from 575 to 560 Ma, which temporally overlaps with the crystallization of the youngest granitoids. Phase equilibrium modeling of metasedimentary granulites from three different localities within the NVC, indicates that all areas record similar peak *P–T* conditions of 750–850 °C and 5300–7500 bar. This is followed by high temperature retrograde evolution to 640–800 °C and 4500–6000 bar. A post-collisional thermal event linked to the intrusion of large norite bodies (520–480 Ma) is recorded in our metagreywackes (monazite U–Pb) and in granites (monazite and zircon U–Pb) from 523 to 495 Ma.

1. Introduction

Nearly two decades after the concept of confined orogens was introduced (Pedrosa-Soares et al., 2001; Rogers and Santosh, 2004), its type example, the Araçuaí Orogen (AO, Brazil), still lacks detailed investigation. Studies on classical (or intercratonic) orogens, such as the Fosdick Complex, West Antarctica (e.g., Korhonen et al., 2012), the Ivrea Zone, Italy, (Barboza and Bergantz, 2000), and the Limpopo Belt, South Africa (e.g., Stevens and van Reenen, 1992; Nicoli et al., 2014; Taylor et al., 2014) have provided a valuable wealth of information on a variety of processes that occur during orogenesis, including high-grade metamorphism, partial melting, melt extraction and emplacement. The investigation of these processes ultimately leads to a better understanding of Earth's crustal evolution through time. But how do they operate in confined orogens? In this study, we begin to address this question by investigating one key unit within the high-grade and crystalline core of the AO: the Nova Venécia Complex (NVC).

The Nova Venécia migmatite-granulite-granite Complex is exposed over an extensive area of the AO core, where high-grade metasedimentary rocks occur in close association with voluminous peraluminous and metaluminous granitoids that

* Corresponding author. Tel.: +1 5852755713.
E-mail address: frichter@ur.rochester.edu (F. Richter).

http://dx.doi.org/10.1016/j.precamres.2015.10.012
0301-9268/

represent pre-, syn- and post-collisonal periods in the Araçuaí orogeny (630–480 Ma, Pedrosa-Soares et al., 2011). Interestingly, the migmatites and granulites preserve a range of high-grade mineral assemblages with little evidence for retrogression.

The novelty of this study consists in the use of combined methods to constrain the nature of these high-grade lithotypes, the ages of metamorphism linked to granite formation and the metamorphic evolution within the NVC, specifically, we use field-based observations, petrography, mineral chemistry, U–Pb LA-ICP-MS geochronology in zircon and monazite and thermodynamic modeling (pseudosections) in order to: (1) constrain the *P–T* evolution of samples; (2) establish why the high-grade rocks record different mineral assemblages; (3) determine a possible source or different sources for high-grade metasedimentary samples based on geochronology; and (4) correlate metamorphic events to intrusion of igneous bodies occurring in close association with the sampled high-grade rocks. This is a contribution to help elucidate crustal processes occurring in the AO, which may also lead to a better understanding of other Gondwana-related orogenic segments today exposed in South America and Africa.

2. Geological setting

The Nova Venécia Complex comprises migmatitic granulite facies metasediments and granitoids located in the high-grade core of the Araçuaí Orogen, in the states of Minas Gerais and Espírito Santo, southeast of Brazil (Fig. 1). The AO is one of the Neoproterozoic-Lower Paleozoic orogenic segments formed diachronously during the Brasiliano-Pan African amalgamation of West Gondwana to the south of the paleo-São Francisco-Congo Craton (Fig. 2). The terranes once merged into West Gondwana landmass were broken apart by the Cretaceous South Atlantic

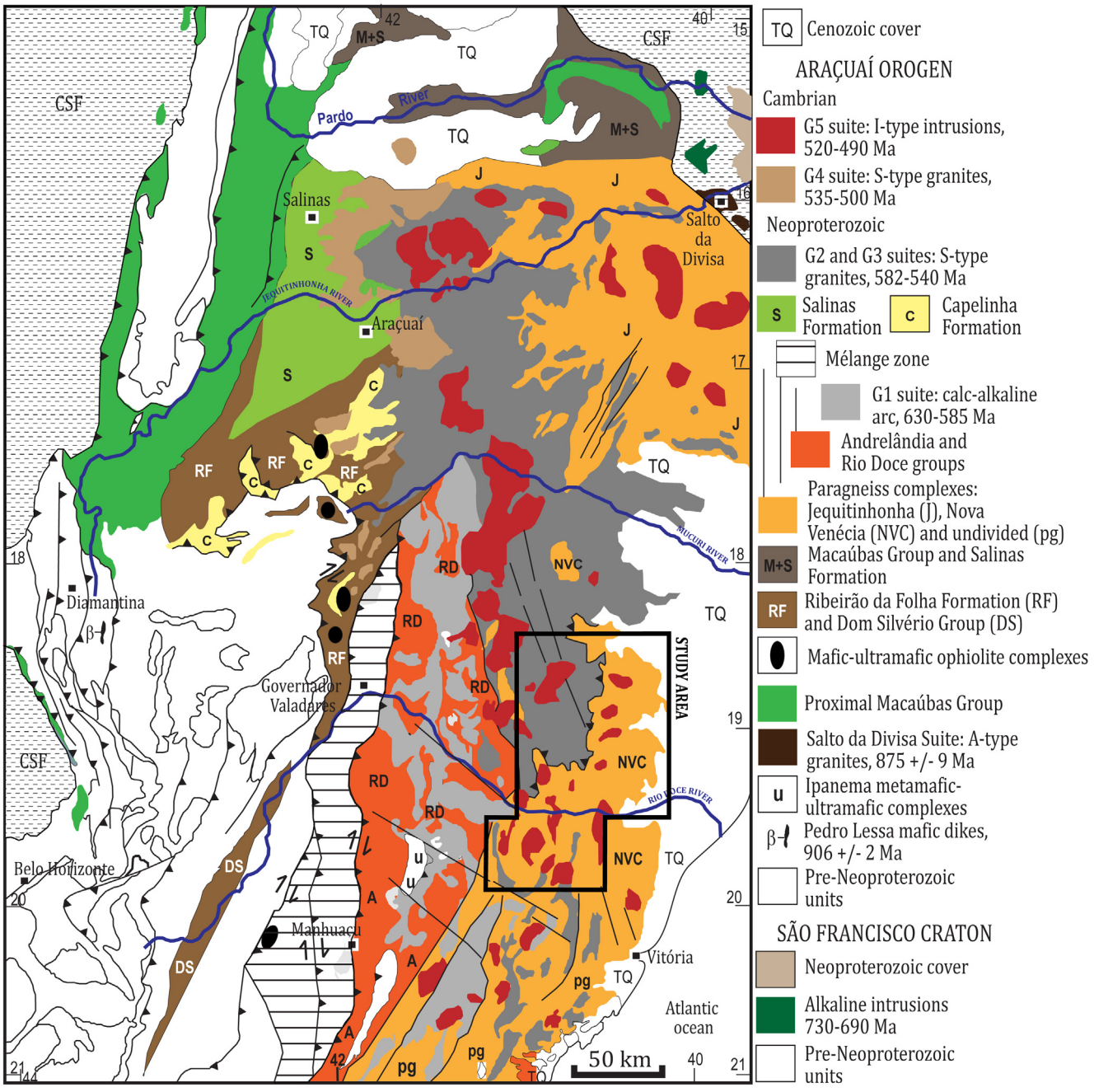

Fig. 1. Geological map of the Araçuaí Orogen and the study area (modified from Pedrosa-Soares et al., 2007).

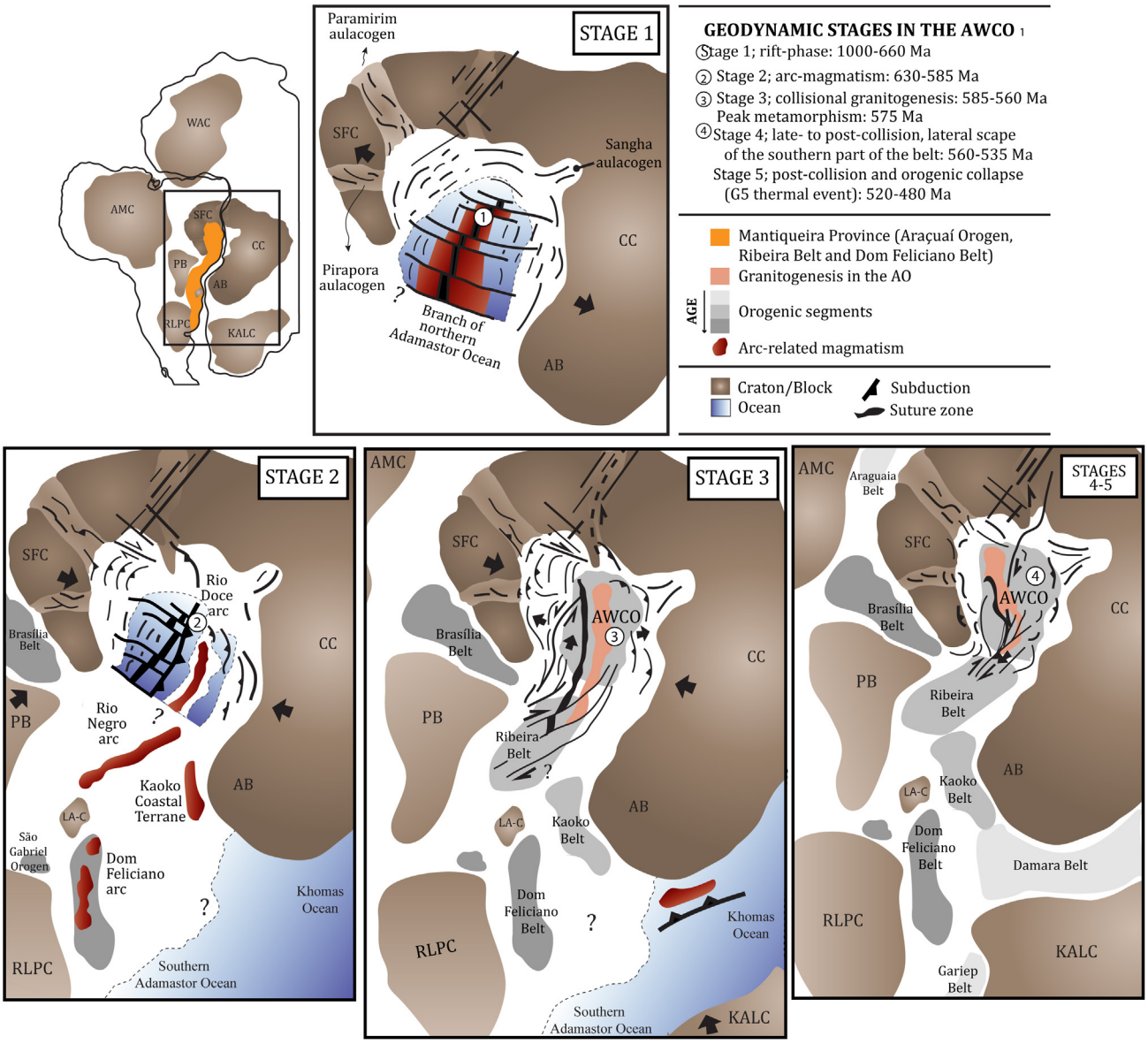

Fig. 2. Cartoon showing a simplified evolution of the Brasiliano-Pan African orogenic system, with emphasis in the Araçuaí-West Congo Orogen (modified from Alkmim et al. (2006). Based on Silva et al. (2005a,b, 2008), Rosa et al. (2007), Queiroga et al. (2007), Trouw et al. (2000), Campos Neto and Caby (2000), Valeriano and Pimentel (2008), Basei et al. (2005), Goscombe et al. (2005), Pedrosa-Soares et al. (2006, 2011), Peixoto et al. (2014), Heilbron and Machado (2003), Gray et al. (2008), Frimmel and Frank (1998), Jung and Mezger (2003), Schmitt et al. (2004) and Bossi and Gaucher (2004). The cratons/blocks include: São Francisco (SFC); Congo (CC); Angola block (AB, depicted as part of the CC); Kalahari (KALC); Amazon (AMC); Paranapanema block (PB); Rio de Plata (RLPC); and Luís Alves-Curitiba Block (LA-C).

rifting and are now complementary orogenic segments exposed in eastern South America and southeastern Africa. Prior to break up, there is evidence that the São Francisco and Congo Cratons remained connected since the Paleoproterozoic by the so-called Bahia-Gabão Bridge (Porada, 1989). This supports the proposal that the Araçuaí Orogen and its complementary segment in Africa, the West Congo Belt, were formed as a confined orogenic system within an embayment of the paleo-São Francisco-Congo Craton, which hosted a gulf of the Adamastor Ocean (Fig. 2; Pedrosa-Soares et al., 2001).

It has been proposed that the Araçuaí-West Congo Orogen (AWCO) evolved in five geodynamic stages (Alkmim et al., 2006; Fig. 2). Most of them are associated with production and emplacement of pre- to post-collisional granitoid Supersuites known as G1–G5 (e.g. Pedrosa-Soares et al., 2006, 2011), as summarized in Table 1, and with deposition to metamorphism of metasedimentary rocks in the AWCO belts and core. The five geodynamic stages consist of: a rift-phase in stage 1 (1000–660 Ma, e.g. Pedrosa-Soares and Alkmim 2011, Silva et al., 2008; Queiroga et al., 2007); the pre-collisional stage 2 (630–575 Ma; Pedrosa-Soares et al., 2011; Silva et al., 2005a; Gonçalves et al., 2014, 2015; Fig. 2); the syn-collisional stage 3 (585–560 Ma; Pedrosa-Soares et al., 2011; Gradim et al., 2014); and the late to post-collisional stages 4 (560–535 Ma) and 5 (520–490 Ma), related to the AO tectonic collapse (Pedrosa-Soares et al., 2006, 2008, 2011; Table 1). A more detailed review on the NVC geological setting and the AO tectonic evolution in relation to other Brasiliano Pan-african orogenic belts can be found in Richter (2015).

3. Previous studies on the NVC metamorphism

Previous studies report that the main rock-types in the NVC are cordierite-rich granulites and biotite + garnet ± cordierite ± orthopyroxene ± sillimanite migmatitic paragneisses (Roncato,

Table 1
Main characteristics of the G1–G5 granitoid Supersuites. Referencing indicated by the numbers in superscript as follows: 1, Roncato (2009); 2, Pedrosa-Soares et al. (2007); 3, Pedrosa-Soares et al. (2011); 4, Gradim et al. (2014); 5, Gonçalves et al. (2015).

	G1	G2	G3	G4	G5
Age (Ma)	630–580[2,5]; 630–585[3]	580–560[2]; 585–560[3]	545–520[2]; 545–525[3]	535–500[2]; 530–500[3]	520–490[2]; 520–480[3]
Stage	Pre-collisional1[1,2,3] to early collisional[4]	Syn-collisional[1,2,3] or late pre-collisional to late collisional[4]	Late to Post-collisional[1,2,3,4]	Post-collisional (orogenic gravitational collapse)[1,2,3,4]	Post-collisional (orogenic gravitational collapse)[1,2,3,4]
Main rock types	Tonalite and granodiorite, minor granite[3,5]	Syenogranite to tonalite and syenogranite to granodiorite[4]	Leucogranite (alkali-granite to syenogranite)[3,4]	Granites, pegmatites[3,4]	Syenogranite to granodiorite, minor norite to enderbite[3,4]
Geoche-mistry	I-type; metaluminous to slighly peraluminous; expanded calc-alkaline[3,4]	Mostly S-type; peraluminous; sub- to calc-alkaline[3]	S-type; peraluminous; high-K alkaline[4]	Mostly S-type; mostly peraluminous; sub-alkaline[3]	I- to A-types; metaluminous to slightly peraluminous; high K-Fe calc-alkaline to alkaline[3,4]
Origin	Plutonism related to the Rio Doce magmatic-arc[2,3]	Generated mostly from anatexis of metassedimentary rocks[2,3]	Generated mostly from anatexis of G2 granites[2,3]	S-type event of granite genesis related to the orogenic gravitational collapse[3]	Predominant mantle contribution; partial re-melting from a mainly metaluminous continental crust; and dehydration melting from slightly peraluminous rocks[3]

2009; Gradim, 2013), which were metamorphosed under upper amphibolite to granulite facies conditions (Gradim, 2013; Munhá et al., 2005). Available peak pressure–temperature estimates from paragneisses assemblages are 5.0–6.1 kbar at 712°C to 930 °C (Gradim, 2013) and 6.5 ± 0.5 kbar at 820 ± 30 °C (Munhá et al., 2005). The suggested age of peak metamorphism in the NVC is 575 Ma (Gradim et al., 2014). To the south of the AO (Fig. 2), in the central-north Ribeira Fold Belt (state of Rio de Janeiro, SE Brazil), it is reported that high-grade metamorphic rocks followed a clockwise *P–T* path from peak conditions of 8 ± 1 kbar and 850 ± 50 °C to retrogression at ca. 500 °C and 5 kbar (Bento dos Santos et al., 2011).

4. Methodology

Twenty-nine samples from eight outcrops located in the Espírito Santo State, Brazil (Fig. 3) were collected for petrographic characterization. Coordinates of all outcrops, their localities, observed lithotypes, and samples collected are given in Appendix B.1. Three metasedimentary samples (101, 7A1B and 3A1) were chosen for metamorphic modeling based on their whole rock chemistry, mineral chemistry and petrography. U–Pb LA-Q-ICP-MS zircon and monazite geochronology data were obtained from metasedimentary samples 3A1, 101, 7A1B, 114 and granitoid samples 7B, 7B. Please refer to Appendices A.1 and A.4 for methods used to obtain mineral chemistry and whole rock chemistry.

The metamorphic conditions in peak and preserved assemblages in three samples of the NVC were investigated using phase equilibrium calculations in the chemical system Na_2O–CaO–K_2O–FeO–MgO–Al_2O_3–SiO_2–H_2O–TiO_2–Fe_2O_3 (NCKFMASHTO) using THERIAK-DOMINO software (De Capitani and Petrakakis, 2010), in combination with the up-dated Holland and Powell (1998) dataset. The modeling used the *a–x* relationships of White et al. (2007) for silicate melt; White et al. (2002) for orthopyroxene, spinel and magnetite; Holland and Powell (2003) for K-feldspar and plagioclase; White et al. (2000, 2005) for ilmenite; White et al. (2005) for garnet and biotite; Holland and Powell (1998) for cordierite. The dataset was compiled for Theriak-Domino by Doug Tinkham. The mineral abbreviations are as follows: Ms – white mica; Bt – biotite; Grt – garnet; Opx – orthopyroxene; Crd – cordierite; Ky – kyanite; Sil – sillimanite; And – andalusite; Pl – plagioclase; Kfs – K-feldspar; Ilm – ilmenite; Mag – spinel; Rt – rutile; H_2O – aqueous fluid; Liq – silicate liquid/melt; Qtz – quartz; Zrc – zircon; Mnz – monazite; Ap – apatite.

The U/Pb data were collected with a New Wave UP-213 coupled with a mass spectrometer Agilent 7700x in the Geology Department of the University of Ouro Preto. In situ monazite dating was performed in sample 114 at the Central Analytical Facility in Stellenbosch University, South Africa, LA-Q-ICP-MS. For detailed descriptions of the analytical method, please refer to Appendices A.2 and A.3 and B.3 and B.4 for U/Pb data. Uncertainties on single spot ages are given at 1σ uncertainties; uncertainties on weighted mean or concordia ages of populations are given at 2σ uncertainties. The data is presented using density concordia diagrams constructed by cumulatively adding the normalized probability density functions (PDF's) of each individual analysis according to their calculated mean values and 2σ uncertainties (Fig. 9). The PDF of each individual spot analysis was calculated using the equation for a bi-variate normal distribution with correlated errors, using the DensityDist code of Pullen et al. (2014) which incorporates a mathematical approach similar to that described in detail by Sircombe (2006). Each of the diagrams in Fig. 9 contains Concordia and mean ages calculated using Isoplot/Ex (Ludwig, 2003). Traditional concordia diagrams presenting the individual ellipses of each analysis at 95% confidence are provided as supplementary material to this article (Appendix C.1).

5. Lithotypes of the NVC and field evidence for partial melting

Table 2 presents the most relevant lithotypes investigated in detail; their name abbreviations used in this study; their mineral assemblages; and the outcrops from where they were collected. All samples are metagraywackes whose protoliths probably contained different amounts of matrix components (Richter, 2015). In the next subsections, we provide a detailed description of these lithotypes and the anatectic features of each outcrop.

5.1. Outcrops 10 and 11

Outcrops 10 and 11 are both located in the city of Colatina (Fig. 3). They expose a gently folded stromatic migmatite, where leucosomes and melanosomes are spaced regularly and oriented parallel to the foliation defined by biotite (Fig. 4(a-1)). This banded sequence may relate to the compositional layering of the protolith. Melanosomes containing fine-grained garnet are in contact with leucosomes containing 2–3 cm medium- and coarse-grained garnet (Fig. 4(a-2)). The assemblages in the melanosomes are represented by BGCM-101 in outcrop 10 and by BGM-114 in outcrop

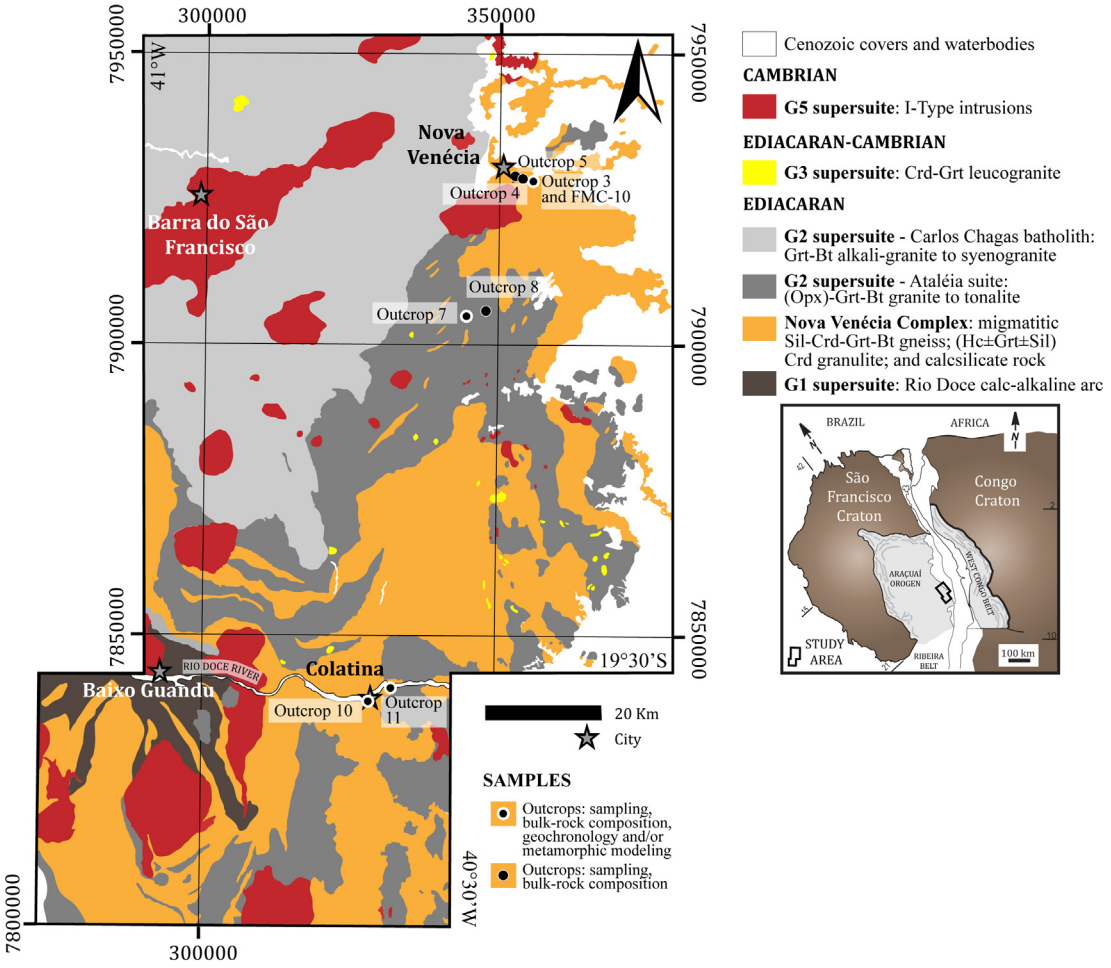

Fig. 3. Geological map of the study area (modified from Gradim, 2013). The outcrops from where samples were collected are: outcrops 3 and FMC10 (samples 3A1, FMC10, 3A4, 3A2, 3A3, 3A5); outcrop 4 (4A1, 4A2); outcrop 5 (5A, 5B); outcrop 7 (7A1B, 7B, 7D, 7A1A, 7A2A, 7A2B, 7C1, 7C2); Outcrop 8 (8A, 8B); outcrop 10 (101, 102, 103); outcrop 11 (114, 111, 112, 113, 116).

Table 2
The main characteristics of the outcrops and samples studied in detail.

Outcrop	Outcrop-scale Main feature	Relevant sampled lithotype	Sample#	Abbreviation used in this study	Mineral assemblage
10	Bt-Grt-Crd metatexite	Biotite-garnet-cordierite metagreywacke	101	BGCM-101	Biotite + garnet + cordierite + sillimanite + plagioclase + K-feldspar + ilmenite + quartz; AP: zircon, monazite and apatite
11	Bt-Grt metatexite	Biotite-garnet metagreywacke	114	BGM-114	Biotite + garnet + sillimanite + plagioclase + K-feldspar + ilmenite + quartz; AP: zircon, monazite and apatite
7	Bt-Grt-Opx metatexite	Biotite-garnet-orthopyroxene metagreywacke	7A1B	BGOM-7A1B	Garnet + orthopyroxene + biotite + plagioclase + K-feldspar + ilmenite + quartz + pyrite; AP: zircon, apatite and monazite
		Peraluminous granodiorite	7D	PG-7D	Garnet + biotite + k-feldspar + plagioclase + quartz; AP: zircon and monazite
		Granite	7B	G-7B	garnet + k-feldspar + plagioclase + quartz; AP: zircon and monazite
3	Crd ± Grt diatexite	Cordierite metagreywacke (known as cordierite granulite)	3A1	CG-3A1	Cordierite + K-feldspar + plagioclase + sillimanite + spinel + ilmenite + biotite + quartz; AP: zircon, monazite and apatite
			3A4	CG-3A4	Cordierite + K-feldspar + plagioclase + sillimanite + spinel + ilmenite + biotite + quartz; AP: zircon, monazite and apatite
FMC10	Crd ± Grt diatexite	Cordierite-garnet metagreywacke (known as cordierite-garnet granulite)	FMC10	CGG-FMC10	Cordierite + garnet + K-feldspar + plagioclase + sillimanite + spinel + ilmenite + biotite; AP: zircon, monazite and apatite

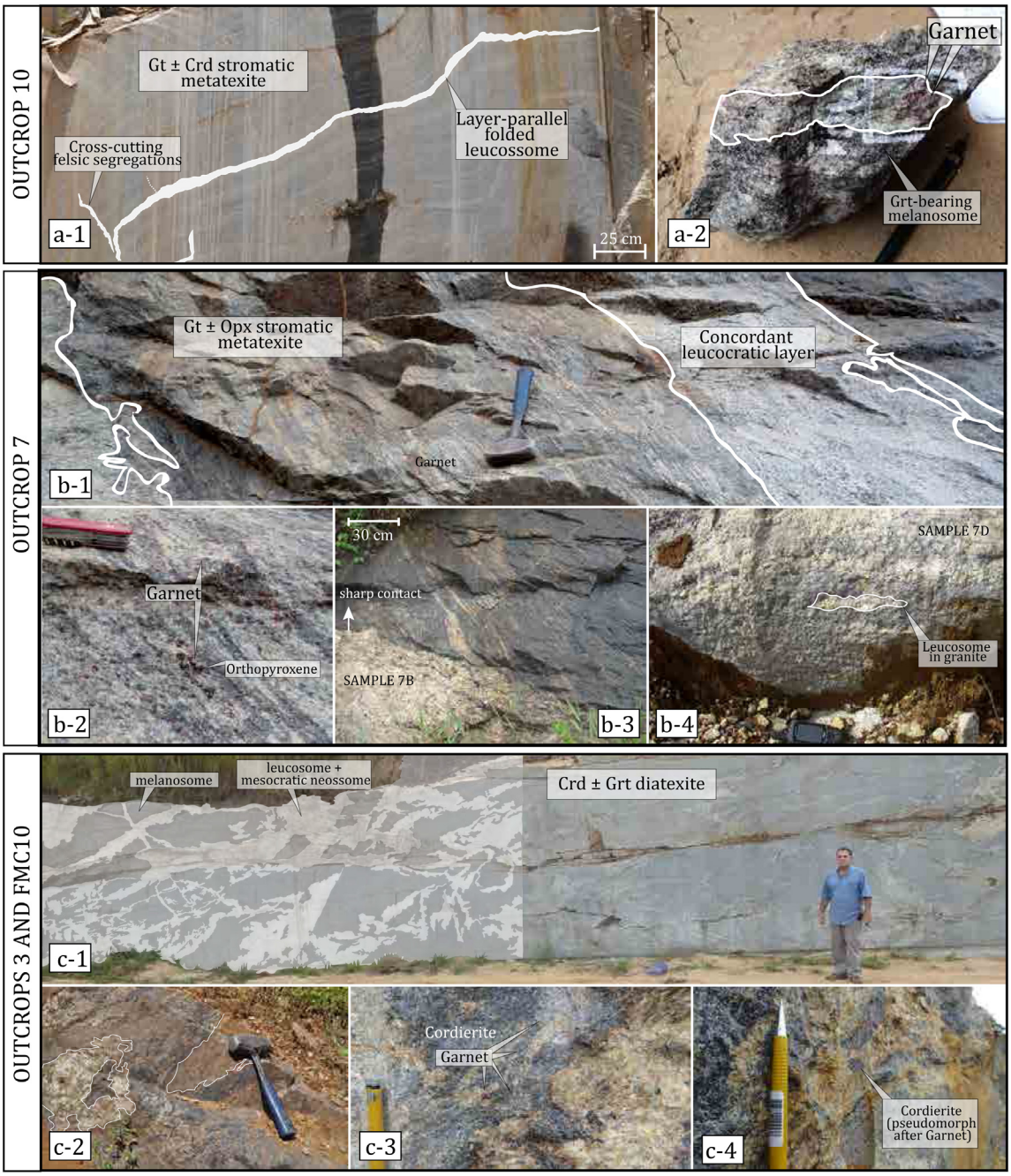

Fig. 4. Anatectic features of the high-grade rocks in outcrop-scale. (a) Outcrop 10. (a-1) Metatexite with folded leucocratic layers oriented parallel to the foliation. Locally, there are cross-cutting felsic segregations (a-4). (a-2) Garnet in leucosomes and melanosomes (sample BGCM-101); (b) Outcrop 7. (b-1) Stromatic (locally folded) metatexite, which bears leucocratic segregations and granitoid intrusions. (b-2) Garnet and orthopyroxene in leucosomes and melanosomes (sample BGOM-7A1B). (b-3) Granitic balloon-shaped dyke intrudes the stromatic migmatite and shows sharp contacts with the host-rock (sample G-7B). (b-4) Some granitic intrusions show evidence of solid-state deformation (foliation oriented parallel to the main layering) and partial melting (sample PG-7D); (c) Outcrops 3 and FMC-10. (c-1) Outcrop FMC-10 exposes a diatexite with a network of interconnected leucocratic segregations. (c-2) Nebulitic leucosome and foliation-paralel mesocratic neosome in outcrop 3, hosted by the melanosome (samples CG-3A1 and CG-3A4). (c-3) In outcrop FMC10, garnet and cordierite are in leucosomes and melanosomes (sample CGG-FMC10). (c-4) Garnet-shaped cordierite in the leucosome.

11 (Table 2). Leucosomes locally cross-cut the foliation, forming a network of interconnected felsic segregations (Fig. 4(a-1)).

5.2. Outcrop 7

Outcrop 7 is located near the community of Vila Fartura (Fig. 3). The outcrop (Fig. 4(b-1)) primarily consists of a stromatic metatexite where the layering of garnet-bearing leucosomes and melanosomes are oriented parallel to the biotite-defined foliation. The mineral assemblage in melanosomes is represented by BGOM-7A1B (Table 2). Rarely, cordierite is present as part of the melanosome, as represented by metasedimentary sample 7C. Orthopyroxene and ubiquitous medium- to coarse-grained garnet are present in both leucosomes and melanosomes, where they are commonly associated (Fig. 4(b-2)).

Four different types of broadly granitic segregations occur at this locality. Firstly, large (>1 m wide) cross-cutting garnet-bearing intrusions with a foliation parallel to the stromatic metaxite. This lithotype is represented by PG-7D (Fig. 4(b-4)), a biotite- and garnet-bearing granodiorite that contains leucosomes

concordant to the migmatite layering, indicating it was also affected by anatexis. Secondly, garnet-bearing, balloon-shaped dykes that cross-cut the stromatic migmatite with sharp contacts and show no evidence of solid-state deformation. This lithotype is represented by G-7B (Fig. 4(b-3)), which consists of coarse-grained quartz-feldspar granite containing a relatively low abundance of fine-grained garnet crystals. Third, garnet-rich leucosomes with patchy morphologies seemingly connected with stromatic leucosomes. Fourth, a large vein-structured leucogranitic dyke that cross-cuts the migmatitic layering.

5.3. Outcrops 3 and FMC10

Outcrops 3 and FMC10 were studied in combination because of their similarities and close spatial association. They are located close to the city of Nova Venécia (Fig. 3), less than 4 km distant from the 15 km wide G5 Pedra do Elefante Batolith (biotite-granite and charnockite; Roncato, 2009). Both outcrops expose a diatexite dominated by networks of interconnected leucosomes and mesocratic neosomes hosted by the melanocratic portion of the exposure (Fig. 4(c-1)). Leucosomes consist of K-feldspar–quartz ± plagioclase and often display patchy and nebulitic morphologies. Melanosomes have very similar assemblages represented by CG-3A1, CG-3A4 and CGG-FMC10 (Table 2) and locally display schollen (Fig. 4(c-1)) and schlieren morphologies (Fig. 4(c-2)). The mesocratic neosome contains the same assemblage with a higher volume of felsic minerals. The sole difference between the outcrops is that in outcrop 3 garnet is rarely observed whereas in outcrop FMC10 garnet is locally present in patchy leucosomes and melanosomes (Fig. 4(c-3)). Inferred cordierite pseudomorphs after garnet occur locally in the leucosomes (Fig. 4(c-4)), where relict garnet is commonly present within cordierite crystals.

6. Petrography, mineral chemistry and whole-rock chemistry

The complete dataset of whole-rock and mineral chemistry is presented in Appendices B.2 and B.5, respectively. Table 3 presents the whole-rock chemistry (in wt% and molar proportions, modified according to modeling) and mineral chemistry of the samples chosen that had good potential for thermodynamic modeling (BGCM-101, BGOM-7A1B and CG-3A1). They share some textures and microstructures despite having different preserved mineral assemblages (Table 2). All samples show textural evidence consistent with the occurrence of partial melting with production and loss of melt to varying degrees, namely (Vernon, 2011; Sawyer, 2008): (1) the presence of small felsic patches, films and veinlets of former melt ("pools of melt" or "protoleucosomes"), now pseudomorphs pseudomorphed by assemblages of quartz, K-feldpar or sodic plagioclase; (2) the pools are developed where the grains of the reactant assemblage touch and are commonly rimmed by grains with euhedral outlines that may be feldspar or peritectic minerals; (3) quartz, K-feldspar or plagioclase often have cuspate rims; (4) the presence of patches and layers rich in peritectic minerals; and (5) reactant minerals have corroded and embayed shapes.

6.1. Biotite–garnet ± cordierite metagreywacke (BGCM-101 and BGM-114)

Here we present the petrography of BGCM-101 (Table 2; Fig. 5(a–e)), which shares most aspects with BGM-114. Subhedral garnet poikiloblasts range in size from 2 to 15 mm in diameter. They contain lobate or rounded inclusions of quartz and biotite, rounded or subhedral and locally myrmekitic inclusions of plagioclase, and elongate to acicular sillimanite inclusions (Fig. 5(b)). Garnet is set in a medium to fine-grained matrix composed of quartz, plagioclase, K-feldspar, cordierite and biotite, which defines the main foliation. Less often, fine-grained subhedral biotite occurs at the rims of garnet (Fig. 5(c)). Garnet crystals are fairly homogeneous in composition (Table 3). Locally, garnet rims less than 150 μm thick with no difference in texture from cores have slightly higher X_{Alm} compositions, e.g. from X_{Alm} = 0.67 in the cores to X_{Alm} = 0.69–0.73 in the rims. Because of these textural relationships and the anatectic features of outcrop 10, garnet is considered to have originated from fluid-absent biotite melting reactions and to be peritectic in origin. Cordierite crystals are commonly poikiloblastic, anhedral, pinitised and 1–7 mm in size. They are often associated with garnet, rimming garnet grains and in instances it appears to be a garnet pseudomorph (Fig. 5(d)). K-feldspar occurs as 2–6 mm subhedral to anhedral crystals that may show embayed shapes and cuspate areas when surrounded by plagioclase, quartz and biotite. They commonly contain included fine-grained euhedral biotite (Fig. 5(e)). Plagioclase is anhedral to subhedral and 1–2 mm in size.

6.2. Biotite-garnet-orthopyroxene metagreywacke (BGOM-7A1B)

BGOM-7A1B (Table 2) consists of poikiloblastic garnet and medium-grained orthopyroxene set in a fine to medium-grained granoblastic matrix of quartz, K-feldspar, plagioclase and biotite, which defines the foliation (Fig. 5(f–k)). Garnet poikiloblasts

Table 3
Representative whole-rock chemistry and mineral chemistry of samples BGCM-101, BGOM-7A1B and CG-3A1, which were used for metamorphic modeling. The H_2O content was modified according to values coherent with the modeling (see text) and normalized to 100%. Complete dataset is in Appendices B.2 and B.5. $X_{Alm} = Fe^{2+}/(Fe^{2+} + Mn)$, $X_{Spss} = Mn/(Fe^{2+} + Mn + Mg + Ca)$, $X_{Grs} = Ca/(Fe^{2+} + Mn + Mg + Ca)$, $Mg\# = 100 \times Mg/(Mg + Fe^{2+})$, $X_{An} = Ca/(Ca + Na + K)$, $X_{San} = K/(Ca + Na + K)$, $X_{FeCrd} = Fe^{2+}/(Mg + Fe^{2+})$.

BGCM-101	Composition (wt%)	SiO_2	TiO_2	Al_2O_3	Fe_2O_3	FeO	MgO	CaO	Na_2O	K_2O	H_2O	Total
		71.72	0.83	12.72	0.34	5.79	2.53	1.52	1.4	2.46	0.67	100
	Composition (molar)	Si	Ti	Al	Fe3	Fe	Mg	Ca	Na	K	H	
		70.91	0.50	14.96	1.56	1.91	2.09	1.55	3.30	2.26	0.95	
	Mineral compositions	Grt X_{Alm}	Grt X_{Grs}	Grt X_{Sps}	Grt Mg#	Crd Mg#	Bt Mg#	Pl X_{An}	Kfs X_{San}			
		0.67–0.73	0.02–0.03	0.02	28–29	67–70	59–65	0.31	0.80–0.88			
BGOM-7A1B	Composition (wt%)	SiO_2	TiO_2	Al_2O_3	Fe_2O_3	FeO	MgO	CaO	Na_2O	K_2O	H_2O	Total
		62.65	0.81	18.79	0.28	4.7	2.24	5.22	3.46	1.63	0.22	100
	Composition (molar)	Si	Ti	Al	Fe3	Fe	Mg	Ca	Na	K	H	
		57.62	0.56	20.37	0.19	3.62	3.07	5.14	6.16	1.92	1.35	
	Mineral compositions	Grt X_{Alm}	Grt X_{Grs}	Grt X_{Sps}	Grt Mg #	Opx X_{FeOpx}	Opx Mg#	Bt Mg#	Pl X_{An}			
		0.64–0.65	0.04	0.03	31	0.48–0.49	50–51	54–60	0.37–0.44			
CG-3A1	Composition (wt%)	SiO_2	TiO_2	Al_2O_3	Fe_2O_3	FeO	MgO	CaO	Na_2O	K_2O	H_2O	Total
		74.57	0.7	13.34	2.18	2.4	1.47	1.52	1.79	1.86	0.15	100
	Composition (molar)	Si	Ti	Al	Fe3	Fe	Mg	Ca	Na	K	H	
		66.30	0.58	13.86	0.24	4.47	3.49	1.50	2.50	2.90	4.13	
	Mineral compositions	Crd Mg#	Crd X_{FeCrd}	Pl X_{An}	Kfs X_{San}	Bt Mg#						
		76–77	0.23–0.24	0.28–0.33	0.73–0.89	65–68						

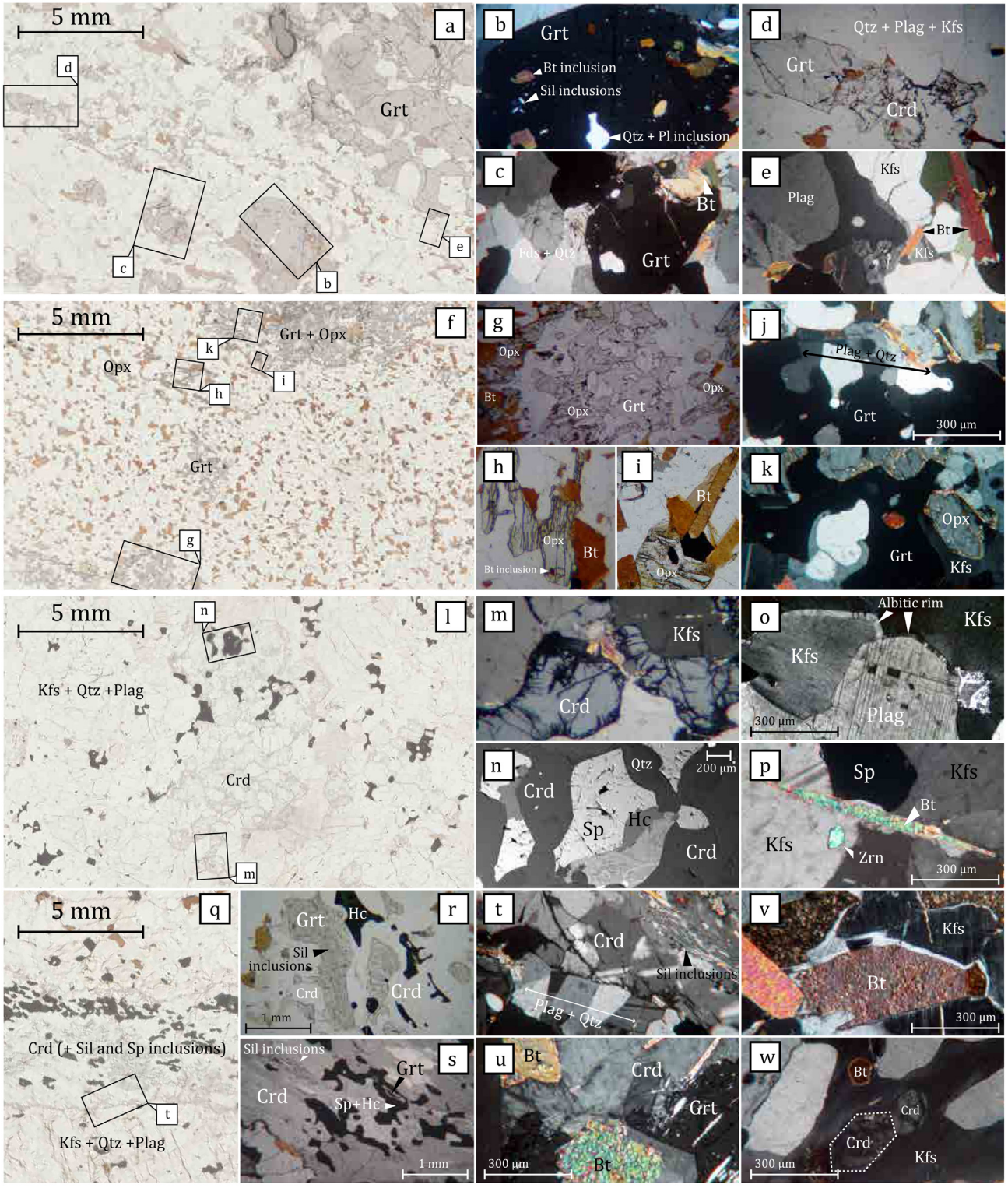

Fig. 5. Petrography of samples observed in thin sections. (a–e) Petrologic aspects of BGCM-101. (a) Part of a scanned thin section from BGCM-101 showing sites from where photomicrographs (b–e) were taken. (f–k) Petrologic aspects of BGOM-7A1B. (f) Part of a scanned thin section from BGOM-7A1B showing sites from where photomicrographs (g–k) were taken. (j) is not showed in (f). (l) and (p) Petrologic aspects of CG-3A1. (l) Part of a scanned thin section from CG-3A1 showing sites from where photomicrographs (m) and (n) were taken. (o) and (p) are not in (l). (q–w) Petrologic aspects of CG-3A4 and CGG-FMC10. (q) Part of a scanned thin section from CG-3A4 showing the site from where photomicrograph (t) was taken. (r, s, u, v, w) are photomicrographs from CGG-FMC10. See text for a more detailed description.

(1–10 mm in diameter) contain inclusions of lobate and rounded quartz, plagioclase and biotite. Garnet compositions are homogeneous and garnet is unzoned (Table 3). Some compositions measured within very thin rims (<150 μm) vary slightly in composition (e.g. from X_{Alm} = 0.64 in cores to 0.65 in rims), although there is no textural difference from cores to rims. Composite Grt + Opx aggregates are common (Fig. 5(f)). Orthopyroxene crystals are fine to medium-grained and are always in contact with either biotite or garnet. Commonly, orthopyroxene contains inclusions either of rounded biotite (Fig. 5(g) and (h)) or fine-grained subhedral

(<200 μm) biotite (Fig. 5(i)). Locally, orthopyroxene associated with garnet has compositions of X_{FeOpx} = 0.45 and Mg# = 54. Together, petrography and field relations suggest that both garnet and orthopyroxene are peritectic phases that formed from fluid-absent melting of biotite. Anhedral 0.4–1.0 mm plagioclase grains are common in the granoblastic matrix and are locally replaced by sericite. Strings of sub- to euhedral Qtz + Pl rim garnet crystals (Fig. 5(j)). K-feldspar is observed either as anhedral crystals in the granoblastic matrix, or as cuspate and lobate crystals rimming orthopyroxene, garnet (Fig. 5(k), feldspar and quartz.

Sample 7C, from the same locality (outcrop 7), bears the same assemblage as BGOM-7A1B, except for the presence of cordierite (1% in volume) and absence of orthopyroxene. Garnet has abundant inclusions of sillimanite, rounded biotite, quartz and plagioclase. Anhedral cordierite rims garnet and biotite and less commonly has rounded biotite inclusions. Locally, cordierite is subhedral.

6.3. Cordierite ± garnet granulite (CG-3A1, CG3A4 and CGG-FMC10)

CG-3A1 is a biotite-poor and garnet-absent lithotype (Table 2) that consists of cordierite poikiloblasts and K-feldspar porphyroblasts set in a granoblastic matrix composed of fine-grained cordierite, K-feldspar, plagioclase, spinel, ilmenite, and minor biotite (Fig. 5(i)). Anhedral, 0.3–10 mm cordierite crystals contain biotite, quartz and spinel inclusions and are commonly pinitized (Fig. 5(m) and (n)). Subhedral ~1 mm cordierite crystals are rimmed by feldspar with cuspate shapes (Fig. 5(l)). K-feldspar occurs as: 0.5–5.0 mm porphyroblasts; 0.1–0.2 mm crystals in the matrix; and anhedral cuspate-shaped crystals embaying spinel, quartz and plagioclase. They are commonly perthitic and show simple twinning. Quartz, plagioclase, biotite, zircon and monazite inclusions occur in K-feldspar poikiloblasts. Anhedral 0.5–2.0 mm diameter plagioclase grains are commonly antiperthitic. Biotite occurs either as inclusions in cordierite and K-feldspar, or as corroded crystals in the matrix (Fig. 5(p)). Spinel consists mainly of magnetite and hercynite. Magnetite is ubiquitous in the matrix, as well as commonly associated with ilmenite and hercynite. Locally, magnetite growth appears to have occurred at the expense of biotite remnant crystals. Hercynite is always associated with crystals of magnetite ± ilmenite within cordierite crystals (Fig. 5(m)).

CG-3A4 is richer in biotite than CG-3A1 (Fig. 5(l) and (q); Table 2). It contains elongate, poikiloblastic coarse-grained cordierite aggregates bearing inclusions of hercynite and sillimanite (Fig. 5(q)). Fine-grained cordierite is less commonly observed in the matrix, where it is more pinitized than cordierite located in elongate aggregates. These aggregates, in addition to relict biotite, define the foliation. Plagioclase + quartz + matrix cordierite locally forms a mosaic rimming elongate cordierite aggregates (Fig. 5(t)).

CGG-FMC10 is a garnet-bearing lithotype (Table 2). Garnet poikiloblasts with sillimanite inclusions are rimmed (Fig. 5(r)) or wrapped (Fig. 5(s)) by hercynitic spinel. Cordierite occurs as coarse-grained poikiloblasts that contain biotite and sillimanite inclusions (Fig. 5(t) and (u)). Either garnet is rimmed by cordierite (Fig. 5(r)) or corroded garnet touches cordierite crystals (Fig. 5(u)). Corroded and subhedral biotite is rimmed by bright segregations that probably consist of feldspar (Fig. 5(v)). Euhedral cordierite is observed in sites where K-feldspar form apparent "pools" rimming other feldspar and quartz with cuspate and lobate shapes (Fig. 5(w)).

The petrography of CG-3A1, CG-3A4 and CGG-FMC-10 and the anatectic features of outcrops 3 and FMC10 suggest that garnet and most cordierite are peritectic in origin, having formed from fluid-absent melting reactions mainly via the breakdown of biotite. However, from petrography, there is evidence that a second metamorphic may have affected those lithotypes and produced some interesting features, specially: newly formed euhedral to subhedral cordierite (Fig. 5(m) and (v)); and anhedral to subhedral hercynite always associated with crystals of magnetite ± ilmenite within cordierite crystals (Fig. 5(q)).

7. *P–T* conditions of equilibrim

7.1. Assessing metamorphic conditions of inferred peak and preserved assemblages

This study focuses on the peak to retrograde evolution of the modeled samples, where granulite grade assemblages are interpreted to have been preserved as a consequence of melt loss. Because the FeO:Fe2O3 ratio and the H2O content in bulk-rock compositions used for modeling play a major role in determining phase relations in pseudosections calculations, a number of T-M_{Fe} and T-MH_2O were constructed for each of the samples in a variety of pressure conditions so their FeO:Fe_2O_3 ratios and H_2O content were consistent with their inferred peak-metamorphic mineral assemblages. H_2O contents were set to values consistent with: (1) the formation of the infered peak-metamorphic assemblages based on the assumption of partial melting driven by biotite-breakdown reactions; (2) the modal abundance of melt between 0 and 10% at peak metamorphic conditions (Nicoli et al., 2014), i.e. values low enough so as to preserve assemblage; (3) the absence of phases at peak which occur only as decompression related textures (e.g., cordierite); (4) the presence of phases at peak conditions that likely have been replaced during decompression considering related textures (e.g., garnet). The bulk-Fe_2O_3 content was chosen to values consistent with the formation of the observed mineral assemblages in determined *P–T* conditions according with the mineral modes and Fe^{3+} contents in garnet and ilmenite. Bulk-rock compositions used for modeling were obtained from those calculations and normalized to 100% (Table 3). Within stability fields, compositional isopleths and isomodes of volume % of phases were plotted with the aim to better constrain *P–T* conditions within peak and preserved assemblage fields. These isopleths were compared to mineral chemistry (Table 3) and isomodes with visually estimated mineral modes.

7.2. Biotite-garnet-cordierite metagreywacke (BGCM-101)

Fig. 6 shows pseudosections calculated for BGCM-101. The *P–T* pseudosection in Fig. 6(a) shows the *P–T* fields of the peak assemblage Bt–Grt–Sil–Pl–Kfs–Ilm–Liq–Qtz and the preserved assemblage Bt–Grt–Crd–Sil–Pl–Kfs–Ilm–Qtz. Fig. 6(b) shows compositional isopleths of X_{Alm} and volume % of Grt. Measured mineral composition of Grt yield X_{Alm} values ranging from 67 (cores) to 73 (>150 μm thin rims) and estimated grt volume of 6–8% delineate two highlighted zones that overlap in the peak field and in the suprasolidus lower-pressure field Bt–Grt–Crd–Pl–Kfs–Ilm–Liq–Qtz. Fig. 6(c) shows compositional Crd Mg# isopleths and volume % of Crd. The two highlighted zones are delineated by measured compositions yielding Crd Mg# that range from 67–70 and cordierite vol% of 2–3. These zones overlap in the Crd-in transition from the peak field to the lower-pressure suprasolidus field and in the preserved assemblage lower-temperature field. Fig. 6(d) shows melt vol% isomodes. The delineated melt vol% zone assumes that no more than 5% was produced at peak. This same procedure was used for the other modeled samples.

7.3. P–T *path and* P–T *conditions of stable assemblages*

The clockwise *P–T* path depicted in Fig. 6(e) was constructed by overlapping all the highlighted zones of Fig. 6(b–d). The peak metamorphic assemblage is stable between 755 to 815 °C and 5900 to >9000 bar. The path starts in the narrow T (~760–780 °C) zone

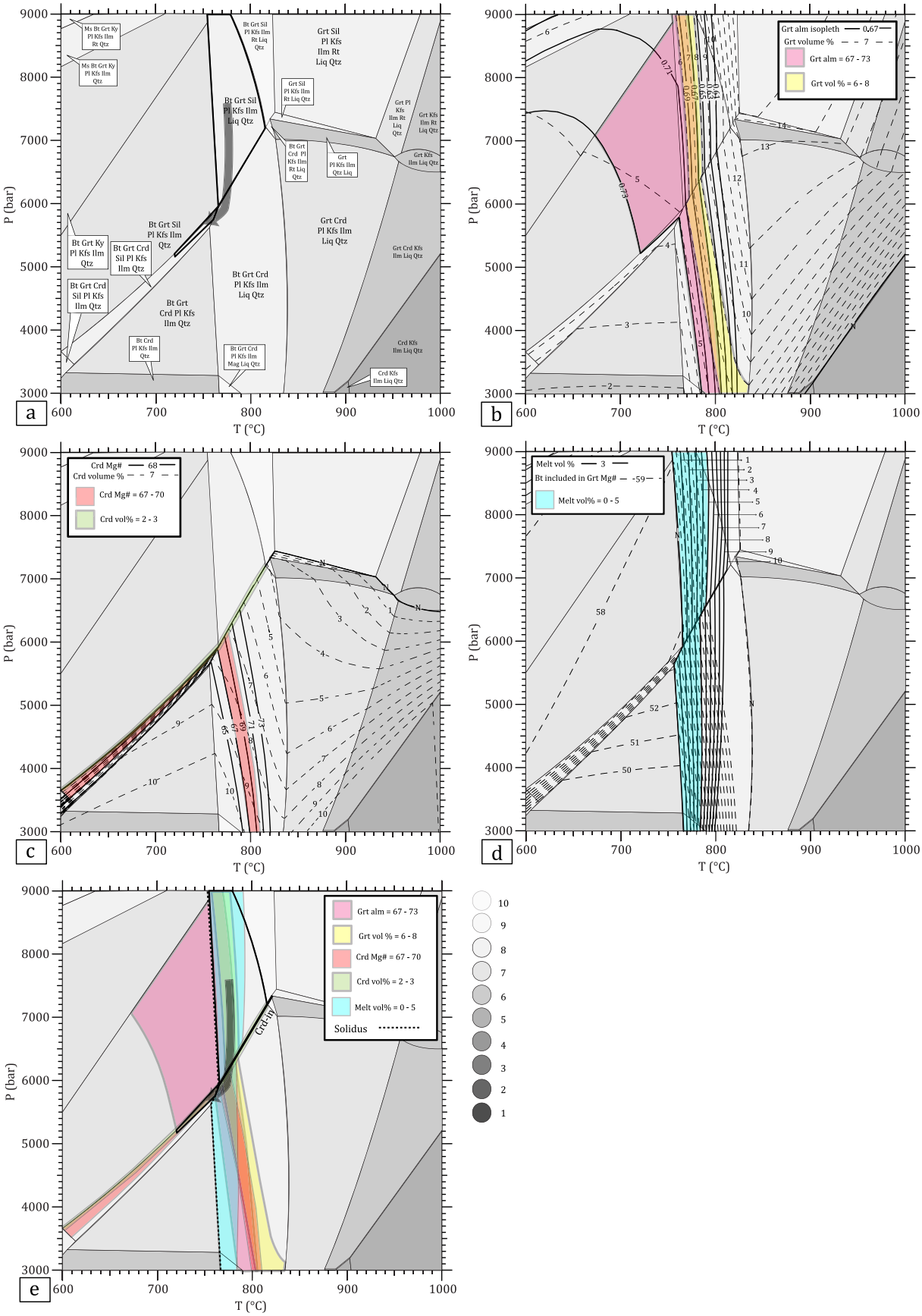

Fig. 6. *P–T* pseudosections calculated for BGCM −101. (a) *P–T* fields of peak assemblage Bt–Grt–Sil–Pl–Kfs–Ilm–Liq–Qtz and the preserved assemblage Bt–Grt–Sil–Pl–Kfs–Ilm–Qtz. It is also shown the inferred *P–T* path obtained from overlapping highlighted zones in (b–d); (b) Compositional isopleths of X_{Alm} and Grt volume % isomodes; (c) Compositional Crd Mg# isopleths and volume % of Crd; (d) Melt vol% and Mg# isopleths obtained from rounded Bt included in Grt; and (e) Overlapping of all the highlighted zones of (b–d) and inferred clockwise *P–T* path. See text for a detailed explanation.

delineated by overlapping zones of Grt vol% (7), Grt X_{Alm} (0.67) and melt vol% (=2–3). Peak conditions are followed by nearly isothermal decompression until the path crosses the Crd-in line and reaches *P–T* conditions where the preserved assemblage is stable. The path crosses part of this field where melt vol% decreases (from 3 to 0), Grt X_{Alm} increases (from 0.71 to 0.73), Grt vol% decreases (from 7 to 5), Crd vol% increases (from 0 to 3) and Crd Mg# decreases (from 70 to 67). This is followed by cooling where the path crosses the solidus (at 765° C and 5800 bar) and reaches the field where the preserved assemblage is stable. Within this field, *P–T* conditions are further restricted by overlapping zones determined by X_{Alm} (thin 150 μm rims = 0.73), Crd Mg# (67–70) and Crd vol% (~2–3). The restricted field within the preserved assemblage field is stable in *P–T* conditions of 720 to 766 °C and 5100 to 5900 bar. This clockwise *P–T* path is consistent with the petrography of the rock and measured mineral chemistry, particularly with cordierite rimming and pseudomorphing garnet (Fig. 6(d)) and with the preservation of the high-grade assemblage with minor evidence of retrogression.

7.4. Biotite-garnet-orthopyroxene metagreywacke (BGOM-7A1B)

Fig. 7 shows pseudosections calculated for BGOM-7A1B. Fig. 7(a) shows *P–T* conditions where the peak assemblage Bt–Grt–Opx–Pl–Kfs–Ilm–Liq–Qtz and the preserved assemblage Bt–Grt–Opx–Pl–Kfs–Ilm–Qtz are stable. This Figure displays a *P–T* path constructed by overlapping highlighted zones in Fig. 7(b–d). Fig. 7(b) shows plots of Grt X_{Alm}, Grt X_{Grs} isopleths and isomodes of Grt vol%. Measured Grt compositions yield X_{Alm} and X_{Grs} values that range from 0.63 to 0.65 and 0.04 to 0.05, respectively. Grt volume in the rock is estimated between 4 and 5%. Within these ranges, the highlighted zones intersect at the subsolidus fields: Bt–Grt–Opx–Pl–Kfs–Ilm–Qtz (preserved assemblage) and Bt–Grt–Crd–Opx–Pl–Kfs–Ilm–Qtz. Fig. 7(c) shows compositional isopleths of Opx Mg# and isomodes of Opx vol%, as well as zones delineated by the measured compositional range of Opx Mg# (50–54) and estimated Opx vol% (3–4). These fields intersect in the peak assemblage field and in the two above-mentioned subsolidus fields. Fig. 7(d) shows melt vol% isomodes from 0 to 5%.

7.5. P–T *path and* P–T *conditions of stable assemblages*

Fig. 7(e) depicts a *P–T* path constructed with the use of overlapped zones in Fig. 7(b–d). The peak assemblage is stable within a narrow field from 810 to 852 °C and 5300 to >9000 bar. The clockwise *P–T* path starts at peak and is followed by decompression and subsequent cooling after the solidus is crossed (at 810 °C and 5300 bar). A suggested restricted field of stability of the preserved assemblage ranging from 630 to 800 °C and 4300 to 5200 bar was constructed by overlapping zones of Grt X_{Alm} (0.63–0.65), Grt X_{Grs} (0.04–0.05), Grt vol% (4–5), Opx Mg# (50–54) and Opx vol% (3–4). After the *P–T* path crosses the solidus and reaches this restricted field, values of Grt X_{Alm} increases from 0.63 to 0.65, Grt X_{Grs} decreases from 0.05 to <0.05, Grt vol% remain in-between 5 and 4, Opx Mg# decreases from 54 to 52 and Opx vol% slightly decreases from ~4 to >4. This decompression and subsequent cooling is consistent with measured compositions in most small garnets and in a few garnet rims of X_{Alm} = 0.64, as well as in matrix orthopyroxene (Mg# = 50) containing fine-grained biotite inclusions (Fig. 7(i)). This is also reflects the slightly decrease in Opx vol% whereas Grt vol% remains roughly the same.

The subsolidus restricted field encompasses part of a lower-pressure Crd-present assemblage (Crd-in line shown as a dashed line within this field), although Crd was not observed as part of the preserved assemblage. In the lower-pressure section of this field, plots of Crd vol% yield less than 1 vol% Crd. It is possible that: (1) such values are so small that may not be represented in thin sections or visible in outcrop-scale; or (2) the dashed Crd-in line in fact represents a low-pressure limit for the stability of the preserved assemblage restricted field. Consistent with this, other samples from the same outcrop (e.g. sample 7C) do contain a few cordierite crystals (approx. 1% vol). Therefore, it would be reasonable to assume that the low-pressure limit for the stability of the preserved assemblage would be from the cordierite-in line until the 1% vol cordierite isomode. In any case, the *P–T* obtained from modeling is consistent with observed microstructures and with the preservation of the high-grade assemblage with minor evidence of retrogression.

7.6. Cordierite granulite (CG-3A1)

In Fig. 8, pseudosections calculated for CG-3A1 show the peak assemblage Grt–Crd–Sil–Pl–Kfs–Ilm–Mag–Liq–Qtz and the preserved assemblage Bt–Crd–Sil–Pl–Kfs–Ilm–Mag–Qtz in (a). The *P–T* path between these assemblages is depicted in Fig. 8(a) and was constructed by overlapping the highlighted zones in Fig. 8(b–d). Fig. 8(b) shows plots of Crd Mg# and Crd vol% isomodes. The measured values of Crd Mg# and estimated Crd vol% delineate two highlighted zones. Fig. 8(c) shows plots of Bt Mg#, Bt vol% and Grt vol%. Although CG-3A1 is a Grt-absent metagreywacke, Grt vol% isomodes were plotted because: (1) CGG-FMC10, collected from the same location, is a Grt-bearing metagreywacke; (2) there is textural evidence in CG-3A1, CG-3A4 and CGG-FMC10 that garnet has been replaced by cordierite and spinel (Fig. 8). In fact, the pseudosection shows that Grt is only stable in suprasolidus fields above ~6000 bar. The measured values of fine-grained biotite Mg# range from 65 to 68 and the estimated modes of 0–3 vol% are consistent with the small amount of Bt observed in thin sections from CG-3A1. Fig. 8(d) shows plots of melt vol% isomodes and Pl X_{an} isopleths. Values of melt% from 0 to 5 and Pl X_{An} from 0.28 to 0.33 delineate two highlighted zones.

7.7. P–T *path and* P–T *conditions of stable assemblages*

The clockwise *P–T* path depicted in Fig. 8(e) was constructed by overlapping zones of Fig. 8(b–d). The peak assemblage is stable between 775 to >1000 °C and 6250 to 7500 bar. The path starts at peak, which is followed by decompression where the path crosses the Grt-out line. Microstuctures corroborate this, particularly in CGG FMC10, where garnet is rimmed and wrapped by spinel (e.g., Fig. 5(r) and (s)) and cordierite locally appears as a garnet pseudomorph (e.g. Fig. 5(l)) and touching corroded garnet (e.g., Fig. 5(u)). This is also consistent with Crd vol% increase until approximately 16% in the field Crd–Sil–Pl–Kfs–Ilm–Mag–Liq–Qtz. The path continues with substantial cooling where it crosses the solidus (at ~780 °C and 5500 bar), the Crd–Sil–Pl–Kfs–Ilm–Mag–Qtz field and reaches the preserved assemblage field. The small field that further restricts *P–T* conditions of equilibria of the preserved assemblage is delineated by a dashed line and represents the overlapping of Crd Mg# and Bt Mg# isopleths. It is stable in *P–T* conditions of 650–720 °C and 4250–5555 bar. This restricted field almost reaches measured values of Pl X_{An} = 0.34. Interestingly, it underestimates the volume of cordierite observed in the rock (12–15%) to 7% whereas it overestimates the amount of Bt (0–3%) to 4%.

The modal abundance of cordierite and the presence of hercynite in CG-3A1, CG-3A4 and CGG-FCM10 are not completely explained by metamorphic modeling but can be assessed from metamorphic microstructures and field relations. The fact those samples were collected from outcrops that are less than 4 km distant from the wide Pedra do Elefante G5 Batholith suggests that the peak-metamorphic mineral assemblages have been modified by a lower pressure metamorphic episode associated with emplacement of this pluton. This has been observed in other

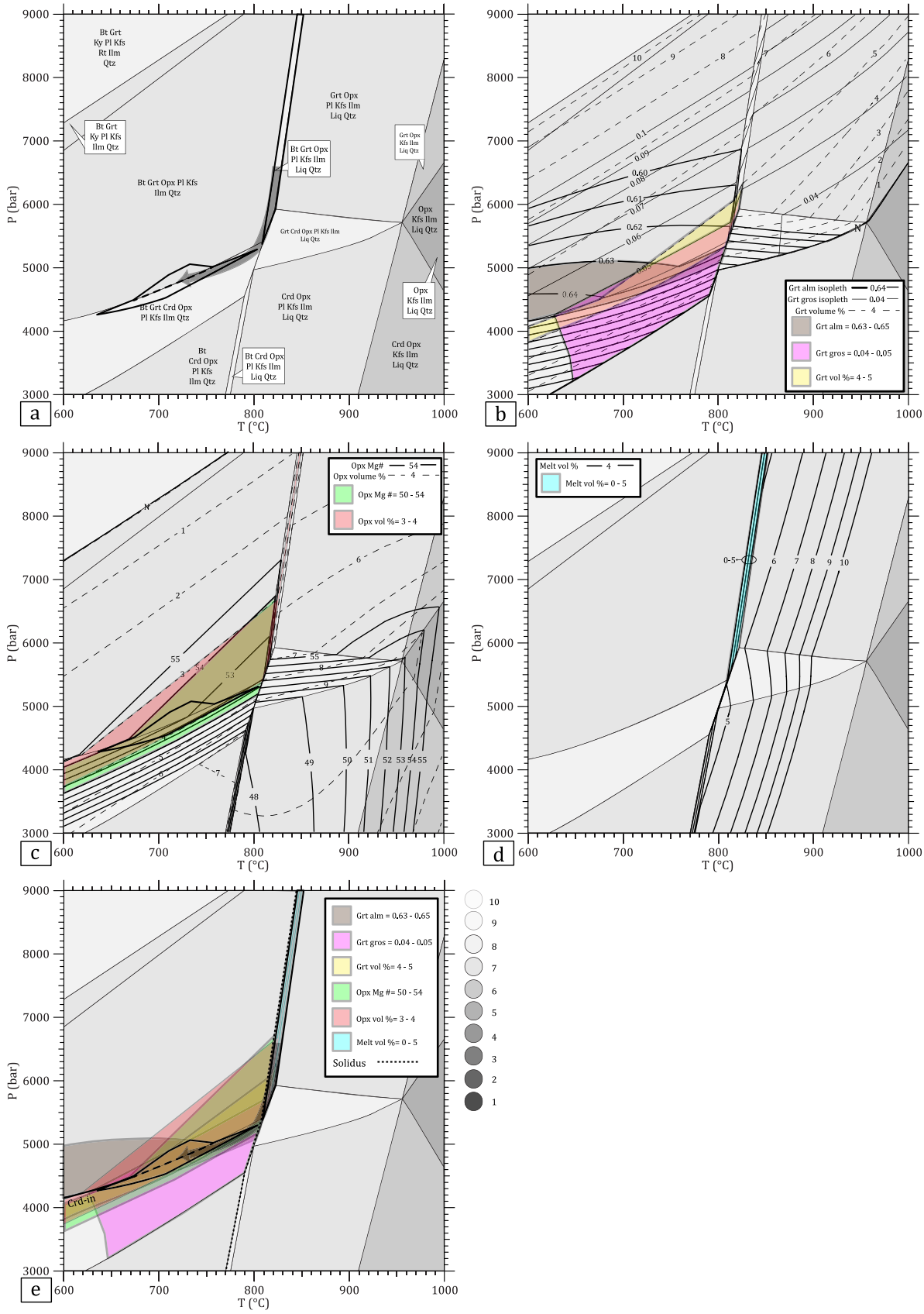

Fig. 7. *P–T* pseudosections calculated for BGOM-7A1B. (a) *P–T* conditions where the peak assemblage Bt–Grt–Opx–Pl–Kfs–Ilm–Liq–Qtz and the preserved assemblage Bt–Grt–Opx–Pl–Kfs–Ilm–Qtz are stable. This Figure displays a *P–T* path constructed by overlapping highlighted zones in (b–d); (b) plots of Grt X_{Alm}, Grt X_{Grs} isopleths and Grt vol % isomodes; (c) compositional isopleths of Opx Mg# and Opx vol%; (d) melt vol % isomodes; (e) clockwise *P–T* path constructed with the use of overlapped zones in Fig. 8(b–d). See text for a detailed explanation.

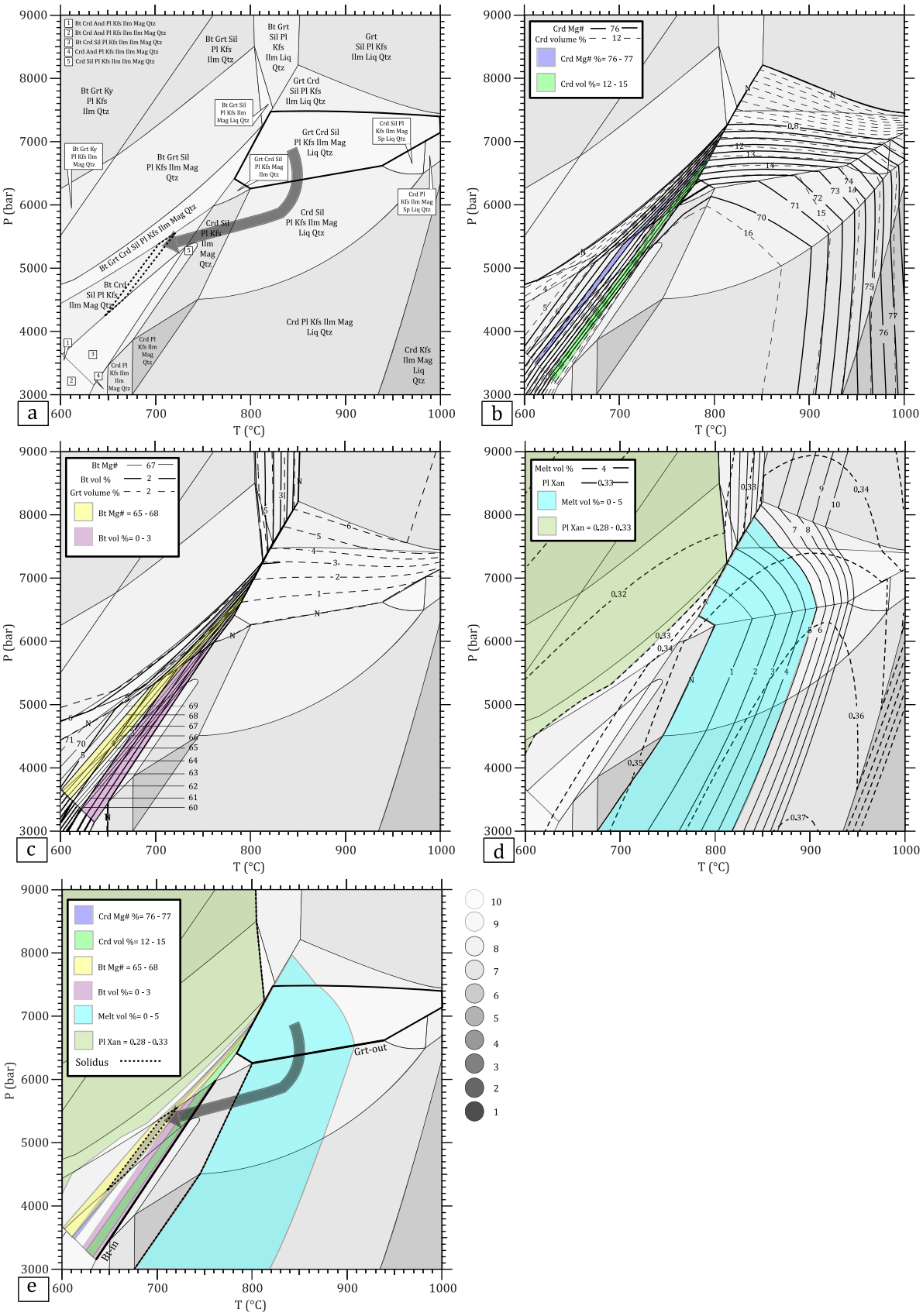

Fig. 8. *P–T* pseudosections calculated for CG-3A1. (a) *P–T* fields of stability of the peak assemblage Grt–Crd–Sil–Pl–Kfs–Ilm–Mag–Liq–Qtz and the preserved assemblage Bt–Crd–Sil–Pl–Kfs–Ilm–Mag–Qtz. The *P–T* path between these assemblages and was constructed by overlapping the highlighted zones in (b-d); (b) Plots of Crd Mg# and Crd vol% isomodes; (c) plots of Bt Mg#, Bt vol% and Grt vol%; (d) Plots of melt vol % and Pl Xan; (e) Clockwise *P–T* path constructed by overlapping zones of (b–d). See text for a detailed explanation.

Table 4
Main populations that compose the zircon detrital dataset and calculated maximum sedimentation ages, which are the Concordia ages of the youngest populations in each sample.

	Sample	Population 1	Population 2	Population 3	Population 4	Population 5	Population 6	Population 7
Detrital populations	7A1B	609.7 ± 3 Ma (60%)	649.2 ± 6 Ma (20%)				822.8 ± 11 Ma (12%)	877.3 ± 14 Ma (8%)
	101	612.3 ± 3 Ma (38%)	652.5 ± 6 Ma (24%)	698.2 ± 7 Ma (21%)		781.1 ± 18 (2%)	807.8 ± 19 Ma (2%)	903.4 ± 7 Ma (13%);
	3A1	612.8 ± 3 Ma (36%)	649.1 ± 4 Ma (34%)	715.4 ± 9 Ma (7%)	746.4 ± 6 Ma (15%)	789.5 ± 7 Ma (8%)		
Maximum sedimentation age	7A1B	606.1 ± 3 Ma (MSWD = 0.91)						
	101	607.3 ± 4 Ma (MSWD = 1.80)						
	3A1	607.4 ± 6 Ma (MSWD = 2.20)						

orogenic segments worldwide, e.g. the Ivrea Zone, Italy (Barboza and Bergantz, 2000). The overprint consists mainly in late generation of cordierite and hercinitic spinel. We speculate that the underestimation of cordierite modes obtained by metamorphic modeling may be justified by the generation of more cordierite post-peak (e.g. Fig. 5(m) and (w)).

8. Zircon and monazite U–Pb geochronology

U–Pb zircon and monazite ages obtained in our study are presented in Fig. 9 and summarized in Tables 4 and 5. Supplementary Figures can be found in Appendices C.1 and C.2 and the complete dataset in Appendix B.3.

8.1. Peraluminous granodiorite (PG-7D)

PG-7D contains zircons that vary in size from 50–100 μm (width) to 50–400 μm (length) and have a variable morphology (Fig. 9(k)). Analysis in 50 spots yield a range of concordant to sub-concordant ages that spread along the Concordia diagram from ca. 631 to 475 Ma (Fig. 9(a)) and record a complex history. The unmix ages routine of Isoplot/Ex (Ludwig, 2003) yields at least 5 populations with ages (±2σ) of 626.0 ± 9 (6%), 594.4 ± 7.8 (14%), 570.6 ± 3 (41%), 508.8 ± 5 (26%) and 483.2 ± 7 (13%) Ma (AppendixC.2(a)). The ages of these populations are consistent with the following described mean ages, Concordia ages and morphologies from this sample and from other samples in this study. CL-defined cores with bright luminescence truncated by darker overgrowths define the oldest population (n = 3) with a mean age of 626.1 ± 8 Ma (MSWD = 0.44; Appendix C.2(a)). Six spots in elongate, prismatic, euhedral to subhedral magmatic zircons with oscillatory zoning (OZ) or faded OZ (that may or may not be truncaded by thin mostly 10 μm rims) yield a Concordia age of 593 ± 8 Ma (MSDW = 2.1, Fig. 9(a)) and Th/U = 0.14–0.46. This age is interpreted to record the magmatic crystallization of the intrusive PG-7D prior to peak regional deformation and metamorphism. The remaining 39 spot analysis was obtained from zircon metamorphic overgrowths (30–70 μm) that have Th/U = 0.04–0.26, are mostly bright luminescent and truncate CL-defined cores with OZ or faded OZ. Twenty-one zircon spots yield a mean age of 571 ± 4 Ma (MSWD = 1.4; Fig. 9(a)). Four spots yield a concordia age of 523.2 ± 9.4 Ma (MSDW = 2.1; Appendix C.2(a)), which is very similar to the magmatic age of the granite sample 7B (Fig. 9(c); see next). Ten spots yield a mean age of 501.9 ± 4 Ma (MSDW = 0.84; Appendix C.2(a)). The remaining four spots have a mean age of 483 ± 6 Ma (MSWD = 0.99; Appendix C.2).

Monazites are 1:2 and 1:1 (100–300 μm in lenght) subhedral to subrounded unzoned grains with very little number of preserved cores, whose spots compose three very distinct age populations (Fig. 9(b)). The oldest one (n = 3) have ages from ca. 663 to 620 Ma that are interpreted as inherited. Twenty-eight spots have mean ages of 566.5 ± 4 Ma (MSWD = 0.86). The youngest population (n = 20) have a mean age of 513.0 ± 4 Ma (MSWD = 0.1).

8.2. Granite (G-7B)

G-7B contains zircons varying in size from 1:2 and 3:5 (50–250 μm in length). Analysis in 81 spots yield a range of concordant to sub-concordant ages that spread along the Concordia diagram from >680 to ca. 486 Ma (Fig. 9(c)). The Unmix ages routine of Isoplot/Ex (Ludwig, 2003) yields 3 younger populations

Table 5
The four groups constrained from zircon and monazite ages from metagreywackes and granites in this study.

		Group 1 – ca. 590 Ma	Group 2 – ca. 570–560 Ma	Group 3 – ca. 520 Ma	Group 4 – ca. 500 Ma
Magmatism	7D	593 ± 8 Ma (MSDW = 2.10; Zr)			
	7B			519.3 ± 2 Ma (MSWD = 1.10; Zr)	
Metamorphism	7A1B	589.6 ± 3 Ma (MSWD = 0.86; Zr)	570 ± 4 Ma (MSWD = 1.60; Zr)		495.0 ± 3 Ma (MSWD = 1.08; Mnz)
	101		560.8 ± 5 Ma (MSWD = 1.16; Zr); 557.4 ± 5 Ma (MSWD = 0.67; Mnz)		498.6 ± 4 Ma (MSDW = 0.94; Mnz)
	3A1		564.6 ± 5 Ma (MSWD = 1.18; Zr)		
	114				502 ± 6 Ma (MSWD = 0.51; Mnz)
	7D		571 ± 4 Ma (MSWD = 1.40; Zr); 566.5 ± 4 Ma (MSWD = 0.86; Mnz)	523.2 ± 9 Ma (MSDW = 2.10; Zr); 513.0 ± 4 Ma (MSWD = 0.10; Mnz)	501.9 ± 4 Ma (MSDW = 0.84; Zr)
	7B				497. 7 ± 4 Ma (MSWD = 1.60; Zr); 506.8 ± 5 Ma (MSWD = 2.20; Mnz)

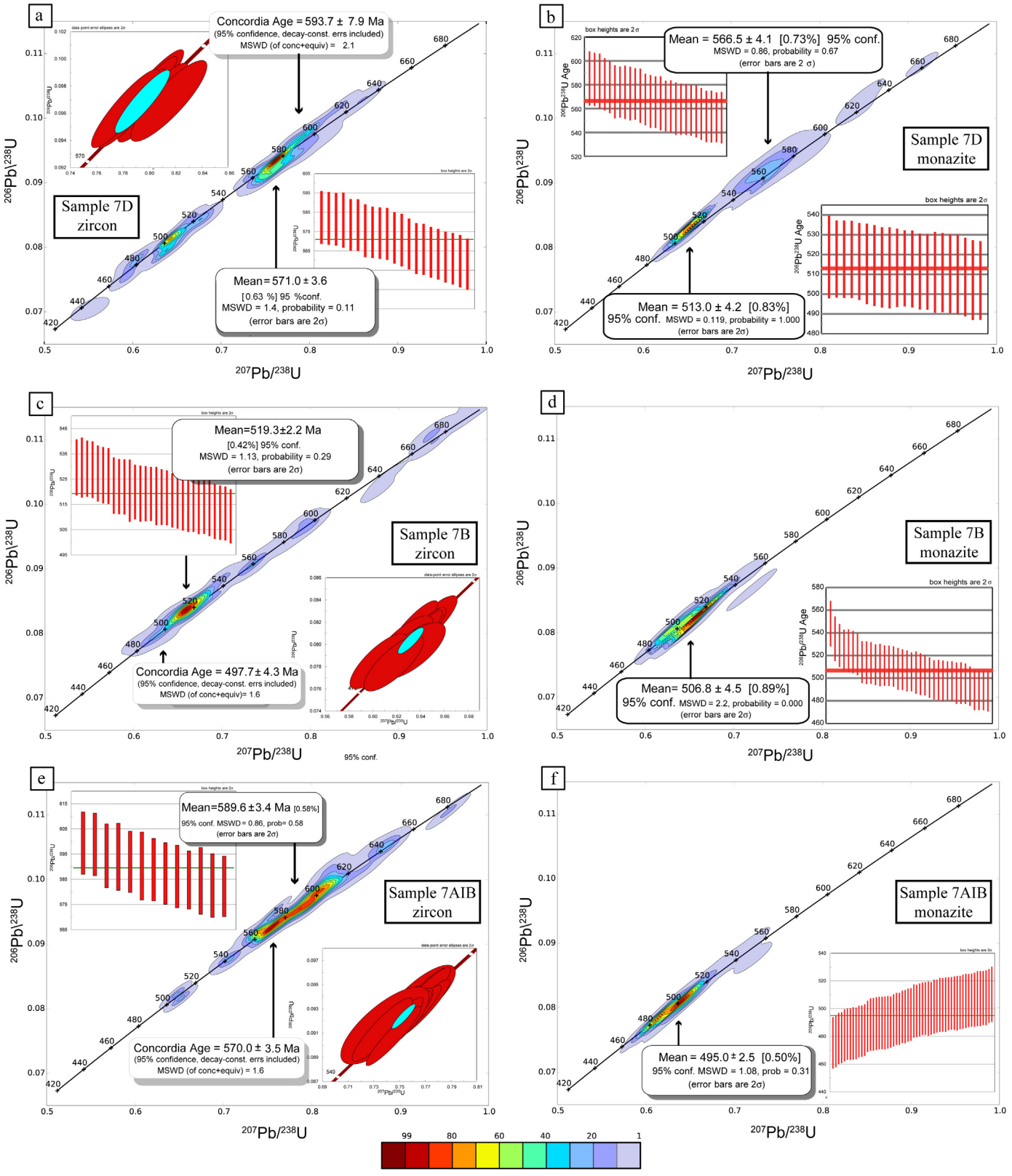

Fig. 9. Density concordia diagrams constructed by cumulatively adding the normalized probability density functions (PDF's) of each individual analysis according to their calculated mean values and 2σ uncertainties. The diagrams contain data from zircons and monazites and conventional Concordia diagrams and mean ages calculated from Isoplot/Ex (Ludwig, 2003) are shown in each of the boxes. (a) and (b) PG-7D; (c–d) G-7B; (e–f) BGOM-7A1B; (g) and (h) BGCM-101; (i) CG-3A1; (j) in situ monazite dating of BGM-114; (k) cathodoluminescence images from PG-7D, G-7B, BGOM-7A1B, BGCM-101 and CG-3A1.

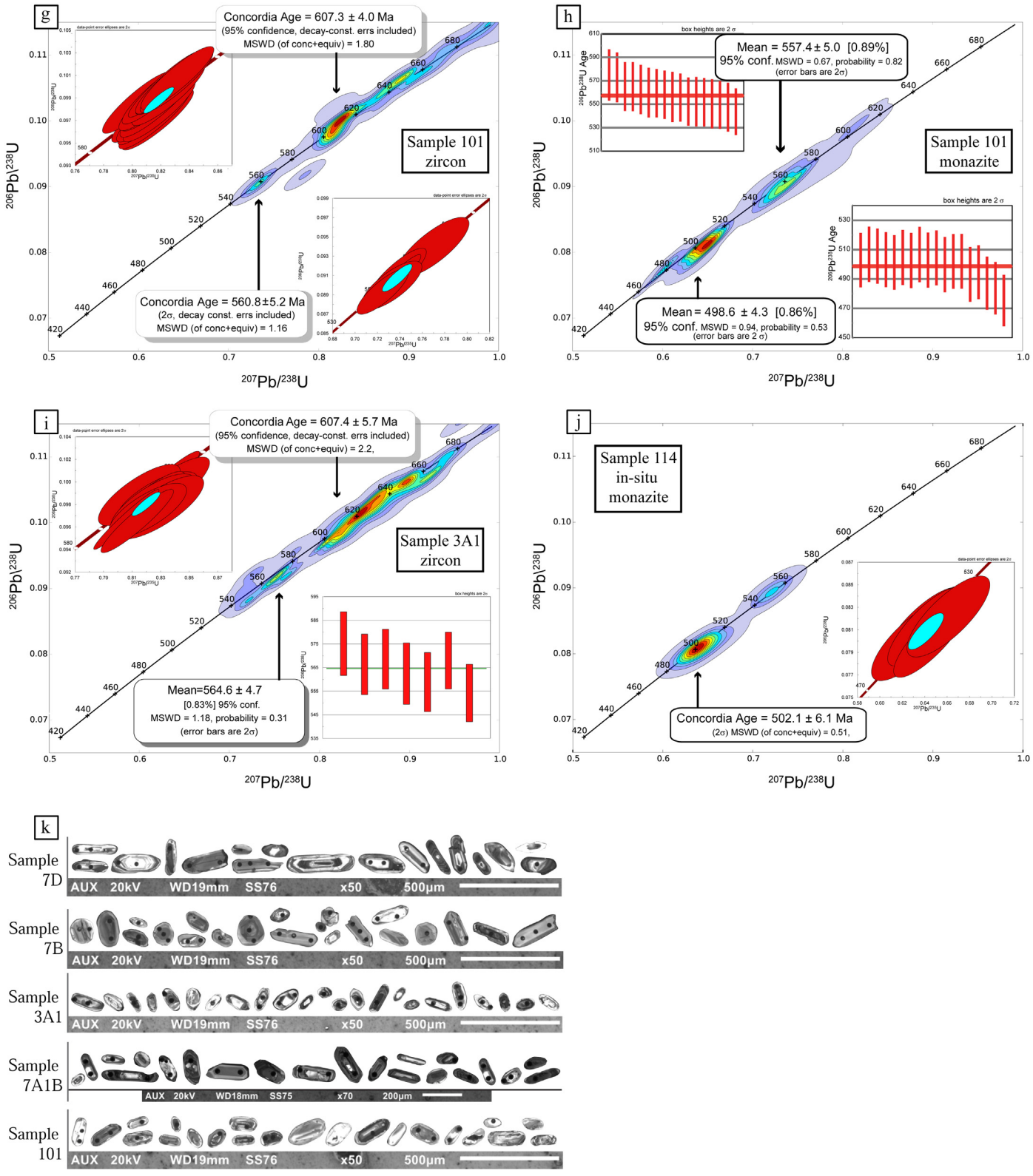

Fig. 9. (*Continued*)

(<600 Ma) with ages (±2σ) of 558.7 ± 5 (17%), 519.9 ± 2 (66%) and 495.7 ± 5 (16%) Ma (Appendix C.2(b)), which are consistent with the following described mean ages, Concordia ages and morphologies from this sample and from other samples in this study (Table 5). CL-defined rounded, mostly dark, 10–80 µm cores, have apparent ages ranging from ca. 2609 to 588 Ma. Analysis in 30 euhedral to subhedral prismatic and/or elongated crystals with faded OZ, that in a few cases overgrow cores, yield a mean age of 519.3 ± 2 Ma (MSWD = 1.1; Fig. 10(c)) and have Th/U = 0.01–0.39. This age is interpreted to record the magmatic crystallization of G-7B, which is undeformed and sharply intrusive in outcrop 7. The zircon cores (inherited and magmatic) are truncated by well defined 20–50 µm

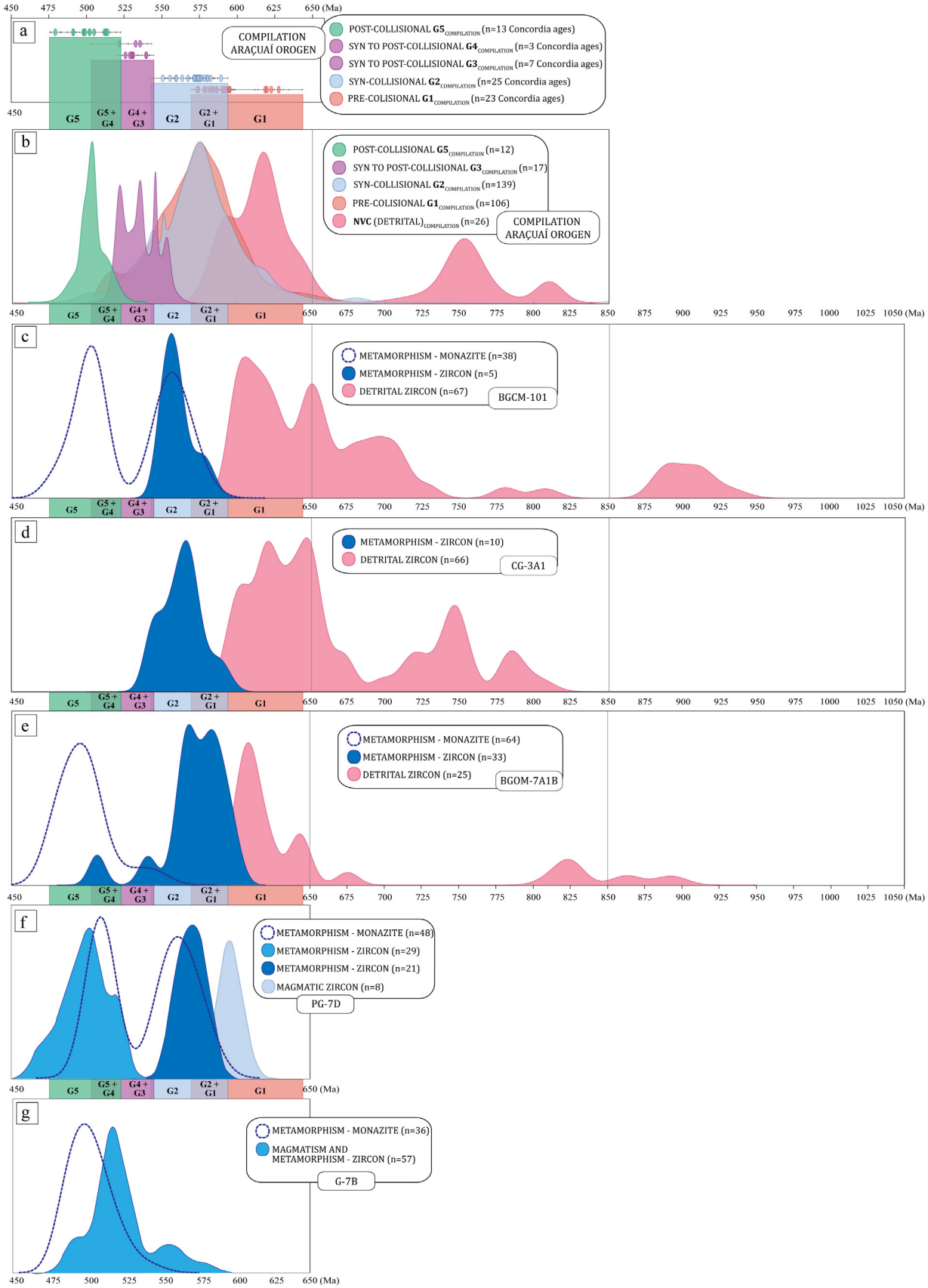

Fig. 10. Probability density plots for zircons and monazites analyzed from metasedimentary and granitic rocks in this study and from compiled data. Diagrams (a–g) show age distributions and the relationship between periods of granitogenesis G1–G5, deposition in the NVC basin and metamorphism. (a) sets of Concordia ages from compilation of data showing periods of granitogenesis G1 to G5 obtained from Silva et al. (2002), Silva et al. (2005a,b, 2007, 2011), Paes (1999), Novo et al. (2010), Novo (2013), Pedrosa-Soares et al. (2011), Noce et al. (2000, 2004), Nalini (1997), Nalini et al. (2000), Baltazar et al. (2010), Figueiredo (2009), Söllner et al. (1991), Whittington et al. (2001), Petitgirard et al. (2009), Roncato (2009), Vauchez et al. (2007), Söllner et al. (1991), Paes et al. (2010), Castañeda et al. (2006), Basílio et al. (2000), Mendes et al. (2005), De Campos et al.

rims that are mostly bright luminescent (Fig. 9(k)). Analysis in eleven of these rims shows one significant youngest population with a Concordia age of 497. 7 ± 4 Ma (MSWD = 1.6; Fig. 9(c)) and Th/U = 0.02–0.20. The meaning of the population at ca. 560 (Fig. 9(c)) in this sample is uncertain, but may record the metamorphic event ranging from 571 to 560 Ma (next subsections) imprinted in all metasedimentary samples and in sample 7D.

Monazites from G-7B are 1:2 and 1:1 (100–300 μm in lenght) subhedral to subrounded unzoned crystals. Fig. 9(d) shows that analysis yield an age range from 548 to 488 Ma along the Concordia line. A mean age of 506.8 ± 5 Ma (MSWD = 2.2) was calculated using the 37 spot analysis within this range. The Unmix ages routine of Isoplot/Ex (Ludwig, 2003) yields three main populations with ages and 2σ uncertainties at 542 ± 25 Ma (4%), 519.8 ± 19 Ma (22%) and 501.7 ± 6 Ma (74%). The age of the two youngest populations (representing 96% of the analysis) are consistent with the supramentioned zircon magmatic ages (519.3 ± 2 Ma) and the zircon youngest metamorphic population (497. 7 ± 4 Ma) in this sample.

8.3. Biotite-garnet-orthopyroxene metagreywacke (BGOM-7A1B)

Zircons from high-grade BGOM-7A1B have a variable morphology, ranging from 1:4 and 3:5 (100–250 μm in lenght) subhedral, elongated to 1:1 (50 μm in length) sub-rounded crystals, which correlate with age groupings. The analysis yield a complex age set that ranges almost continuously from ca. 660 to 530 Ma (Fig. 9(e)) along the corcondia line. CL-defined detrital cores are 2:5 and 1:5 (50–100 μm in length) domains that mostly present ghost OZ. Twenty-five spot ages in cores reveal an apparent span from ca. 873 to 600 Ma. The Unmix ages rotine of Isoplot/Ex (Ludwig, 2003) indicate there are 4 main populations of detrital zircons within this range, with ages (±2σ) of 877.3 ± 14 Ma (8%); 822.8 ± 11 Ma (12%); 649.2 ± 6 Ma (20%); and 609.7 ± 3 Ma (60%; Appendix C.2(c)). These peak ages are clear in the probability density diagram constructed using Isoplot/Ex (Ludwig, 2003) in Fig. 10(e). The youngest spots (n = 12) among detrital zircons yield a concordia age of 606.1 ± 3.4 Ma (MSWD = 0.91; Appendix C.2), interpreted to represent the maximum sedimentation age of sample 7A1B. The CL-defined cores are truncated by both dark and bright luminescent rims that overgrow cores and/or present a transgressive recrystallization over cores. Analysis in rim domains indicates distinct metamorphic populations. The Unmix ages rotine of Isoplot/Ex (Ludwig, 2003) indicate there are 2 (out of 4, Appendix C.2) more important populations of metamorphic zircons within this range at: 587.8 ± 4 Ma (46%) and 568.4 ± 4 (42%). The oldest population (n = 13) have a mean age of 589.6 ± 3 Ma (MSWD = 0.86; Th/U = 0.09–0.28; Fig. 9(e)), interpreted to record the intrusion and magmatic crystallization of early granitoids, such as PG-7D (593 ± 8 Ma), prior to peak deformation/metamorphism. A metamorphic population obtained from 16 zircon spots have a Concordia age of 570 ± 4 Ma (MSWD = 1.6; Th/U = 0.03–0.29; Fig. 9(e)) is interpreted to represent the regional peak metamorphism, which is also recorded in PG-7D (571 ± 4 Ma).

Monazite grains are subhedral and subrounded 1:1 100–200 μm (in length) grains that are unzoned in BSE images. A monazite concordia diagram is presented in Fig. 9(f), from 64 analyzed monazite spots. Fifty-six of the youngest zircon spots yield a mean age of 495.0 ± 3 Ma (MSWD = 1.08).

8.4. Biotite-garnet-cordierite metagreywacke (BGCM-101)

Zircons from BGCM-101 have variable morphologies, including 1:1 and 2:5 (50–250 in length) elongate, subhedral, subrounded and oval crystals. Ubiquotous CL-defined zircon cores, truncated by overgrowths and transgressive recrystallization of rims, are mostly dark 25–100 μm (in length) oval to sub-rounded shaped domains. Sixty-seven analysis in these cores reveal an apparent range of spot ages from ca. 2097 to 597 Ma. Using the Unmix ages routine (Isoplot/Ex; Ludwig, 2003), six main populations are determined among detrital zircons (ages ±2σ): 903.4 ± 7 Ma (13%); 807.8 ± 19 Ma (2%); 781.1 ± 18 (2%); 698.2 ± 7 Ma (21%); 652.5 ± 6 Ma (24%); and 612.3 ± 3 Ma (38%; Appendix C.2(d)). These populations are crearly shown in the probability density diagram of Fig. 10(c). A concordia age of the youngest population (n = 19) is 607.3 ± 4 Ma (MSWD = 1.80), interpreted to be the maximum sedimentation age of sample 101. The zircon rims are 20–50 μm bright domais that overgrow cores, with Th/U = 0.03–0.21. Analysis (n = 5) yield a metamorphic Concordia age of 560.8 ± 5 Ma (MSWD = 1.16; Fig. 9(g)), interpreted to represent the peak regional metamorphism.

Monazites are mostly unzoned rounded 1:1100–200 μm (in length) crystals. Three analysis have ages around 608 Ma, interpreted to be detrital. Two very distinct age populations have were obtained: the oldest (n = 16) with a mean age of 557.4 ± 5 Ma (MSWD = 0.67) and the youngest (n = 18) with a mean age of 498.6 ± 4 Ma (MSDW = 0.94).

8.5. Cordierite granulite (CG-3A1)

Zircons from metasedimentary sample 3A1 are oval to subrounded 1:1 and 1:2 (50–200 in length) crystals. Ubiquotous CL-defined cores are both dark and bright luminescent 50 μm domains that often present ghost OZ. Analysis in these cores yield an apparent range of spot ages spanning from ca. 1942 to 588 Ma. Using the Unmix ages routine (Isoplot/Ex; Ludwig, 2003), six main detrital populations are determined within the most important range from ca. 806 to 588 Ma (ages ±2σ): 789.5 ± 7 Ma (8%); 746.4 ± 6 Ma (15%); 715.4 ± 9 Ma (7%); 649.1 ± 4 Ma (34%); and 612.8 ± 3 Ma (36%). These peak ages are clear in the probability density diagram constructed using Isoplot/Ex (Ludwig, 2003) in Fig. 10(d). The youngest group (n = 10) yield a Concordia age of 607.4 ± 5.7 Ma (MSWD = 2.2; Fig. 9(g)), interpreted to represent the maximum sedimentation age of sample 3A1. Rims are 10–50 μm both dark and bright domains that truncate and recrystallize transgressively over cores. Analysis in seven of these domains yields a mean age of 564.6 ± 5 Ma (MSWD = 1.18), interpreted to represent the peak regional metamorphism. These domains have a variable Th/U ratio from 0.01 to 0.43.

(2004); (b) probability density plots for detrital zircons in NVC metasedimentary rocks and magmatic zircons from granitoids G1–G5 in the Araçuaí Orogen. Data is compiled from Noce et al. (2004); Gradim (2013); Pedrosa-Soares et al. (2011); Petitgirard et al. (2009); Roncato (2009); Gradim (2013); Novo et al. (2010); (c) probability density plots for detrital zircons, metamorphic zircons and metamorphic monazites analyzed in metasedimentary sample 101; (d) probability density plots for detrital zircons and metamorphic zircons analyzed in metasedimentary sample 3A1; (e) probability density plots for detrital zircons, metamorphic zircons and metamorphic monazites analyzed in metasedimentary sample 7A1B; (f) probability density plots for magmatic and metamorphic zircons and metamorphic monazites analyzed in granite sample 7D; (g) probability density plots for metamorphic zircons and metamorphic monazites analyzed in granite sample 7B. The accessory phases are named metamorphic because they record the metamorphism that formed the S-type granite. All probability density curves were constructed using Isoplot/Ex (Ludwig, 2003) by: assigning a normal (Gaussian) distribution to each analysis that is less than 15% (compiled data) and 2% (our data) discordant, based on 206U/238Pb reported ages and 1σ uncertainties; and summing the probability distribution of each acceptable analysis into a single curve.

8.6. Biotite-garnet metagreywacke (BGM-114)

In situ monazite dating was undertaken in BGM-114. BSE images show that monazite crystals are unzoned, range from 20 to 120 μm in size and are included or rimming biotite, garnet and feldspar. Analyses in 7 spots yield a concordia age of 502 ± 6 Ma (MSWD = 0.51; Fig. 9(j)).

9. Discussion and concluding remarks

9.1. Magmatism in the Araçuaí Orogen

In the diagram shown in Fig. 10(a), sets of 71 reported zircon concordia ages from G1 to G5 Supersuites have a broad age overlap, which can be interpreted as a nearly continuous supply of magma from at least 640–480 Ma. Major peaks in zircon crystallization are grouped into six periods: 640–595 Ma (G1 event); 595–570 Ma (G2 + G1 events); 570–540 Ma (G2); 540–525 Ma (G3 + G4); 525–505 Ma (G4 + G5); and 505–475 Ma (G5). Relative probability density (RPD) diagrams constructed using compiled G1–G5 ages (Fig. 10(b)) corroborate these overlaps and further suggest two main magmatic pulses: one that comprise the most voluminous G1 and G2 Supersuites, both with a peak at ca. 575 Ma; and the late event comprising the G5 Supersuite.

9.2. Nature and provenance of the Nova Venécia Complex

The seven populations that compose the NVC detrital zircon dataset (Table 4) are correlated with the main peaks in detrital ages depicted in Fig. 10(c–e). Populations 1 (ca. 609–612 Ma) and 2 (ca. 649–652 Ma), which are the main detrital populations in all of our samples, clearly overlap with the early AO magmatism (Fig. 10(a) and (b)). This indicates the Rio Doce arc (e.g. Pedrosa-Soares et al., 2011), represented by the early G1 plutonism, as the main provenance of NVC protoliths from ca. 650 to 610 Ma (Fig. 12), although minor sources could also be the southern Rio Negro arc (RFB, 650–610 Ma; Heilbron and Machado, 2003; Fig. 10(a) and (b)). This corroborates previous suggestions that the NVC represents a back-arc basin related to the Rio Doce magmatic arc, including the Serra da Bolivia Complex (Heilbron et al., 2013; Novo, 2013) and the (early) G1 Supersuite (Gradim et al., 2014). Older populations 3 (ca. 715–698 Ma), 5 (ca. 789–781 Ma) and 7 (ca. 903–877 Ma; Table 4) may correlate to reported ages of the rift-related Southern Bahia alkaline province (732–696 Ma, Rosa et al., 2007), the early portion of the Rio Negro magmatic arc in the RFB (ca. 790 Ma, Tupinambá et al., 2012) and the rift-related Salto da Divisa Suite (ca. 880 Ma, Silva et al., 2008). Provenance of populations 4 (ca. 746 Ma) and 6 (ca. 807–822 Ma) is uncertain.

The maximum sedimentation age of the NVC is 606 Ma (Table 4). The NVC sedimentation can be bracketed between its maximum depositional age at ca. 606 Ma and the intrusion of granitoids at 593 Ma (PG-7D, Fig. 9(a)). This indicates the NVC was deposited within at most a 13 Ma period, during a transition from pre- (G1) to syn-collisional (G2) plutonism, as shown in Fig. 10(b) and 12. Our interpretation is that the NVC protoliths were (meta)greywackes (enriched with more or less 15–50% clay and silt components), possibly formed as turbidites (high energy density flows) from the Rio Doce magmatic arc.

Although the evolution of the AO and of the RFB occurred, intuitively, in conjunction, there are surprisingly few studies that address this combined evolution. Detrital zircon ages of paragneisses from the southeastern portion of the Neoproterozoic-Ordovician Central Ribeira Orogen reported recently by Fernandes et al. (2015) are very similar to most ages presented in this study. In that region, the majoriy of detrital zircon grains have Neoproterozoic sources divided in three broad groups, which can be correlated to the populations in our study: (1) their 1.0–0.9 Ga sources can be correlated to our Population 7; (2) their 0.9–0.8 Ga sources may correlate with our Populations 5 and 6, which are possibly eroded sources; and (3) their most abundant sources from 750 to 570 Ma can be correlated to our most abundant populations 1, 2, 3 and 4. Fernandes et al. (2015) proposed an evolution for the eastern part of the RFB in two stages, where the first stage represents an extensional setting of Buzios basin and the second a convergent setting at ca. 590–550 Ma. If this is so, the first event could represent a back-arc basin in the RFB that is nearly contemporaneous to the Nova Venecia back-arc basin.

9.3. Metamorphism in the Nova Venécia Complex

Outcrop-scale observations show metatexites and diatexites with leucosomes and melanosomes both containing variable amounts of peritectic garnet, cordierite and orthopyroxene (Fig. 4). Microstructures provide evidence of the former presence of melt and for the formation of peritectic minerals (Fig. 5). Notably, major crustal melting in peraluminous metasedimentary protoliths involves incongruent reactions consisting of muscovite then biotite breakdown, producing high-grade assemblages that commonly contain peritectic sillimanite, garnet, cordierite and orthopyroxene (e.g., Clemens, 2006; Brown, 2007; Taylor et al., 2014). These assemblages and the proportion of melt produced by incongruent reactions depend on *P–T* conditions and protolith compositions. Different protoliths will produce different melt volumes (e.g. Brown, 2007) and different assemblages along a given *P–T–t* path. As H_2O strongly partitions into the melt, melt segregation and escape is required for the preservation of largely unretrogressed high-grade assemblages (e.g. White and Powell, 2002), with leucosomes acting as sites of melt accumulation and melt drainage. Therefore, in this study, the preservation of high-grade assemblages is assumed to have followed melt loss at, or close to, peak *P–T* conditions (e.g. White and Powell, 2002; Taylor et al., 2014; Nicoli et al., 2014). Modeling of all samples show the solidus just below the peak *P–T* assemblages, which is consistent with the preservation of these assemblages (White and Powell, 2002).

The thermodynamic modeling presented in Figs. 6–8 suggests that all samples depict a similar *P–T* path, recording peak *P–T* conditions from approx. 750–850 °C and 5300–7500 bar and conditions of stability of preserved assemblages from approx. 640–800 °C and 4500–6000 bar. Fig. 11 shows their simplified metamorphic evolution. The metamorphic peak in all samples was attained at granulite-facies conditions and all preserved assemblages equilibrated close to the transition between upper amphibolite to granulite conditions. CG-3A1 and BGOM-7A1B record very similar peak *P–T* conditions constrained by the T interval of biotite fluid-absent melting reactions. Although BGCM-101 records lower peak T conditions (an area in-between the T interval of muscovite and biotite fluid-absent melting reactions), there is ubiquitous evidence that reactions taking place in this rock-type are typical fluid-absent biotite breakdown reactions (e.g. Fig. 5(a) and (b)).

Based on evidence from metamorphic modeling, petrography and geochronology of our samples, we interpret that significant exhumation and cooling occurred subsequently to peak metamorphism, but prior to the G5 thermal event (520–480 Ma; AO tectonic collapse). First, G-7B (519 Ma) sharply intrudes the NVC showing no evidence of solid-state deformation related to peak nor any anatectic features linked to the exposed migmatites. Thus it is inferred that the metatexite exposed in outcrop 7 had already cooled by the time it was intruded. Based on the metamorphic modeling of BGOM-7A1B, cooling follows/accompanies decompression. Second, our samples located close to the G5 Pedra do Elefante

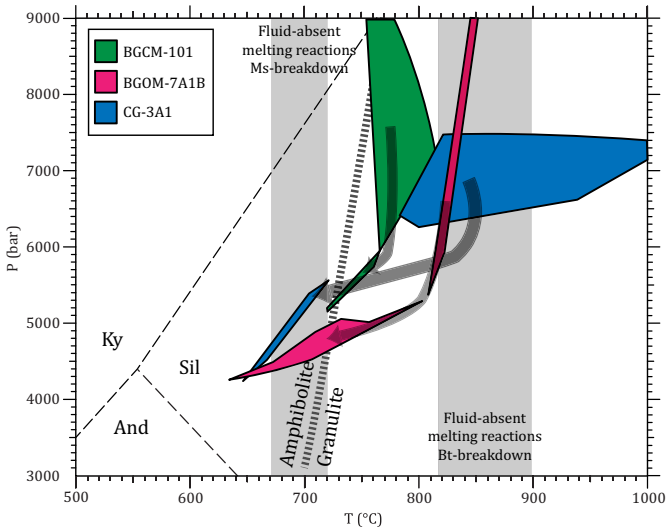

Fig. 11. Suggested and simplified metamorphic evolution for all samples related to granulite and amphibolite conditions of metamorphism and to temperature intervals where biotite and muscovite breakdown most likely occur (Vielzeuf and Holloway, 1988; Patiño Douce and Johnston, 1991; Montel and Vielzeuf, 1997; Stevens et al., 1997; Pickering and Johnston, 1998). Peak metamorphism in all samples was attained at granulite conditions and all preserved assemblages must have equilibrated close to the transition between upper amphibolite to granulite conditions.

Batolith (CG-3A1, CG-3A4, CGG-FMC10) record a late Low Pressure-High Temperature metamorphic event, similarly to other reports from the AO (Pedrosa-Soares et al., 2011), probably occurring from 520–480 Ma. The evidence consists of newly-formed euhedral to subhedral cordierite (Fig. 5(l, v)) and the presence of anhedral to subhedral hercynitic spinel, always associated with crystals of magnetite ± ilmenite within cordierite crystals (Fig. 5(m)). In the metamorphic model of sample CG-3A1 (Fig. 8), the underestimation of cordierite modes within the preserved assemblage field may indicate that the generation of more cordierite post-peak is required to attain observed mineral volumes in cordierite granulites.

Therefore, there are two reasons why metagreywackes record different assemblages: (1) their protolith compositions, also reflected by the different constitution in percentage of each detrital population in each sample (Table 4) and (2) some of the samples were affected by two metamorphic events. The events are the regional granulitic-peak metamorphism (575–560 Ma, next subsection), recorded in all samples, and a younger event dated at ca. 500 Ma (Table 5), recorded in samples from outcrops 3 and FMC10. We infer a second event based on the younger ages (ca. 500 Ma, Table 5) obtained in this study in both metasedimentary rocks and granites, which may relate to massive I-type G5 intrusions (e.g. the Pedra do Elefante Batolith). As previously suggested by Pedrosa-Soares et al. (2011), this may indicate restricted metamorphism within contact aureoles, which is analogous to the metamorphic events affecting the Ivre Zone, in northern Italy (Barboza and Bergantz, 2000). However, it may be that other lithotypes in the AO were also affected by the G5 event but do not contain a strong textural overprint due to their refractory nature following the peak metamorphic event.

9.4. Metamorphic history of the Araçuaí Orogen as recorded by the Nova Venécia Complex

Metamorphism recorded in zircons and monazites in our samples can be grouped into 4 periods, as presented in Table 5. Group 1 (ca. 590 Ma) is recorded in outcrop 7, where the magmatic crystallization of PG-7D can be related to metamorphism recorded in zircons from BGOM-7A1B. This group is interpreted to record an early period of peraluminous magmatism, within the 595–570 Ma range of G1 + G2 plutonism (Fig. 10(a) and (b)). Group 2 is recorded by metamorphic zircons and monazites in BGOM-7A1B, BGCM-101, CG-3A1 and G-7D. In this study, this group is interpreted to represent the AO peak metamorphism ranging from ca. 571 to 560 Ma, causing partial melting in both metagreywackes and early granites (e.g. PG-7D; Fig. 4). Notwithstanding the complexities of the regional geology, it seems reasonable to assume that peak regional metamorphism in the Araçuaí Orogen lasted 15 My, between 575 and 560 Ma, through combining the peak ages determined in previous studies (575 Ma, e.g. De Campos et al., 2004; Gradim et al., 2014) and those obtained here. This period is similar to the period of peak granulitic metamorphism in the central-north part of the Ribeira Belt (575–560 Ma; Bento dos Santos et al., 2011). Notably, these ages partly overlap with the syn-collisional period of magmatism (G1 + G2, 595–570 Ma) with a peak at ca. 575 Ma (Fig. 10(a) and (b)). This suggests a relationship between the peak regional metamorphism recorded in our samples and the youngest portion of the G1 + G2 plutonism, which needs further detailed investigation. We infer that the products of partial melting generated during peak throughout the AO could be at least part of the granitoids contemporaneous to G2 (570–540 Ma) and G3 + G4 (540–525 Ma) periods (Fig. 12). This agrees with the suggestion of Bento dos Santos et al. (2015) that, in the Northern RFB and AO, magmatism took place at 584–544 Ma and metamorphism at 587–560 Ma within a syn-orogenic period. The ages are also very similar to the ages reported by Fernandes et al. (2015) for the stage of convergence in the Buzios basin (590–550 Ma), eastern portion of the RFB. In our study, however, late granitogenesis and metamorphism is also remarkably significant. For instance, in outcrop 7, the sharply intrusive G-7B records magmatic crystallization at ca. 519.3 ± 2 Ma, which is registered by metamorphic-related zircon age of 523.2 ± 9 Ma and monazite age of 513.0 ± 4 Ma in PG-7D (Group 3, Table 5). It is interesting to note that these ages are very similar to the ages reported for the Buzios Cambrian Orogeny (530–510 Ma; Schmitt et al., 2004), to the south. In addition, Group 4 represents the G5 thermal event at ca. 500 Ma, recorded in metagreywackes (monazites) and in granites (monazites and zircons). We infer that ages at ca. 523–495 Ma are linked to partial dissolution of peak 575–560 Ma zircon and monazite in restricted partial melts and then re-precipitation of new anatectic zircon and monazite. Moreover, during this period, CG-3A1, CG-3A4 and CGG-FMC10 were affected by a late metamorphic event. Therefore, we suggest that the supply of magma arising from deep crustal levels throughout the AO was probably continuous from syn- to post-collisional periods (Fig. 10(a) and (b)), it was more significant during ca. 590–560 Ma and 520–480 Ma and possibly caused two main events of metamorphism in the orogen.

The fact that the AO records such a long-lived heat supply history may be related to both or at least one of the following reasons: its evolution as a confined orogenic system (Pedrosa-Soares et al., 2001) and the multiple events of accretion and collision occurring to its south, in the RFB. Several studies in the recent past have used the concept of channelized lower crustal flow to account for the characteristics of large and hot orogenic belts related to magmatism, high-grade metamorphism (partial melting) and deformation of continental crust (e.g., Clark et al., 2005; Royden, 1996; Vanderhaeghe and Teyssier, 2001). In the channel flow model, differential crustal thickness or density contrasts within the crust (contrast in gravitational potential energy) could drive channelized flow of weak, low-viscous (partially melted) layer in the lower crust. This could allow for the transfer of material over distances of more than 100 km (Clark et al., 2005). Considering the clear evidence for widespread partial melting in the AO, we

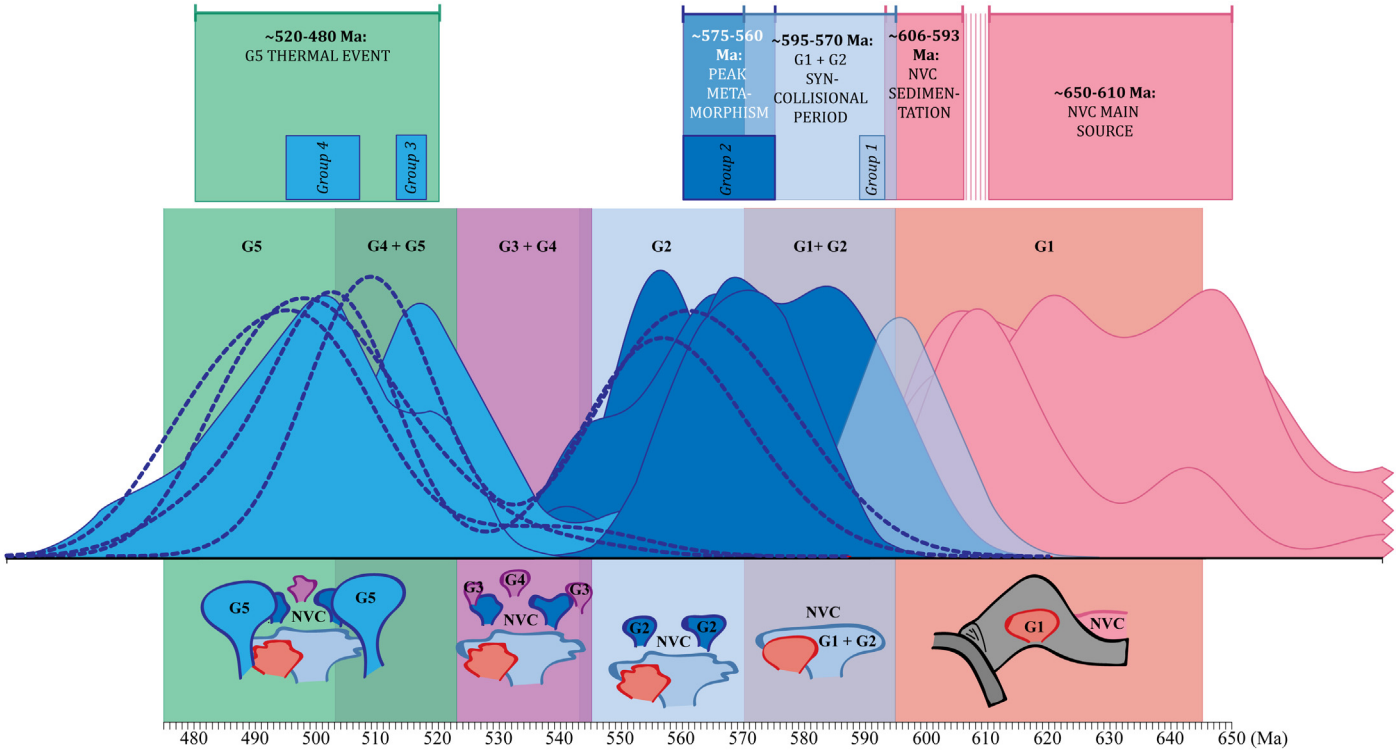

Fig. 12. Summary of findings in this study: correlation between ages of magmatic and metamorphic events recorded in metagreywackes and granites and the periods of main events occurring in the AO. (1) refer to discussion for details; (2) groups presented in Table 5; (3) populations presented in Table 4; (4) overlap of probability density diagrams presented in Fig. 10.

infer that this crustal layer may have represented a weak layer that could have behaved as a viscous flow in a channel, but could not be transferred over long distances due to the confined character of the AO. Obstacles for channelized flows exist, for instance, in the eastern Tibetan Plateau margin (see mechanisms in Clark et al., 2005). Therefore, the confinement of hot material would favor its accumulation near the paleo-arc and Hinterland, increasing the heat flow in the area. Complementarily, the multiple events of accretion and collision in the RFB, may have contributed with some of the heat input in the AO, as many orogenic segments in both systems could (and should) be considered as correlate sections. These hypotheses may represent interesting opportunities for new research in the area.

Acknowledgements

We appreciate financial support provided by: Fundação de Amparo à Pesquisa do Estado de Minas Gerais (FAPEMIG-VALE CRA RDP-00063/10; APQ03943, RDP 0067-10); Financiadora de Estudos e Projetos (FINEP CT-INFRA); and Conselho Nacional de Desenvolvimento Científico e Tecnológico (CNPq 402852/2012-5; 401334/2012-0; 302633/2011-1). G. Stevens gratefully acknowledges NRF support through the SARChI programme. We thank Dirk Frei (Stellenbosch University) for his support in the in situ monazite analysis. F. Richter benefited from MSc scholarship provided by CNPq. We thank the two anonymous reviewers for their insightful comments and suggestions.

Appendix A. Supplementary data

Supplementary data associated with this article can be found, in the online version, at http://dx.doi.org/10.1016/j.precamres.2015.10.012.

References

Alkmim, F.F., Marshak, S., Pedrosa-Soares, A.C., Peres, G.G., Cruz, S.C.P., Whittington, A., 2006. Kinematic evolution of the Araçuaí-West Congo orogen in Brazil and Africa: nutcracker tectonics during the Neoproterozoic assembly of Gondwana. Precambrian Res. 149, 43–64, http://dx.doi.org/10.1016/j.precamres.2006.06.007.

Baltazar, O.F., Zuchetti, M., Oliveira, S.A.M., Scandolara, J., Silva, L.C., 2010. Folhas São Gabriel da Palha e Linhares. Nota explicativa. Programa Geologia do Brasil, CPRM – Serviço Geológico do Brasil, Available from: www.geobank.sa.cprm.gov.br.

Barboza, S.A., Bergantz, G.W., 2000. Metamorphism and anatexis in the mafic complex contact aureole. Ivrea zone, northern Italy. J. Petrol. 41, 1307–1327, http://dx.doi.org/10.1093/petrology/41.8.1307.

Basei, M.A.S., Frimmel, H.E., Nutman, A.P., Preciozzi, F., Jacob, J., 2005. The connection between the Neoproterozoic Dom Feliciano (Brazil/Uruguay) and Gariep (Namibia/South Africa) orogenic belts. Precambrian Res. 139, 139–221.

Basílio, M., Pedrosa-Soares, A.C., Evangelista, H.J., 2000. Depósitos de alexandrita de Malacacheta. Minas Gerais. Geonomos 8, 47–54.

Bento dos Santos, T., Munhá, J., Tassinari, C., Fonseca, P., Dias Neto, C., 2011. Metamorphic P-T evolution of granulites in central Ribeira Fold Belt, SE Brazil. Geosci. J. 15 (1), 27–51.

Bento dos Santos, T.M., Tassinari, C.C.G., Fonseca, P.E., 2015. Diachronic collision, slab break-off and long-term high thermal flux inthe Brasiliano-Pan-African orogeny: implications for the geodynamicevolution of the Mantiqueira Province. Precambrian Res. 260, 1–22, http://dx.doi.org/10.1016/j.precamres.2014.12.018.

Bossi, J., Gaucher, C., 2004. The Cuchilla Dionisio Terrane, Uruguay: an allochtonous block accreted in the Cambrian to SW Gondwana. Gondwana Res. 7 (3), 661–674.

Brown, M., 2007. Crustal melting and melt extraction, ascent and emplacement in orogens: mechanisms and consequences. J. Geol. Soc. Lond., http://dx.doi.org/10.1144/0016-76492006-171.

Campos Neto, M.D.C., Caby, R., 2000. Terrane accretion and upward extrusion of high-pressure granulites in the Neoproterozoic nappes of southeast Brazil: petrologic and structural constraints. Tectonics 19, 669–687, http://dx.doi.org/10.1029/1999TC900065.

Castañeda, C., Pedrosa-Soares, A.C., Belém, J., Gradim, D., Dias, P.H.A., Medeiros, S.R., Oliveira, L., 2006. Geologia da Folha Ecoporanga 1:100.000. CPRM-Serviço Geológico do Brasil, UFMG-Programa Geologia do Brasil, Rio de Janeiro.

Clark, M.K., Bush, J., Royden, L.H., 2005. Dynamic topography produced by lower crustal flow against rheologic strength heterogeneities bordering the Tibetan Plateau. Geophys. J. Int., http://dx.doi.org/10.1111/j.1365-246X.2005.02580.x.

Clemens, J.D., 2006. Melting of the continental crust: fluid regimes, melting reactions, and source-rock fertility. In: Brown, M., Rushmer, T. (Eds.), Evolution and

Differentiation of the Continental Crust. Cambridge University Press, Cambridge, pp. 297–331.
De Campos, C.P., Mendes, J.C., Ludka, I.P., de Medeiros, S.R., de Moura, J.C., Wallfass, C., 2004. A review of the Brasiliano magmatism in southern Espírito Santo, Brazil, with emphasis on post-collisional magmatism. J. Virtual Explor. 17, http://dx.doi.org/10.3809/jvirtex.2004.00106.
De Capitani, C., Petrakakis, K., 2010. The computation of equilibrium assemblage diagrams with Theriak/Domino software. Am. Miner. 95, 1006–1016, http://dx.doi.org/10.2138/am.2010.3354.
Fernandes, G.L.F., Schmitt, R.S., Bongiolo, E.M., Basei, M.A.S., Mendes, J.C., 2015. Unraveling the tectonic evolution of a Neoproterozoic-Cambrianactive margin in the Ribeira Orogen (Se Brazil): U–Pb and Lu-Hfprovenance data. Precambrian Res. 266, 337–360.
Figueiredo, C.M., 2009. O Arco Magmático Brasiliano na conexão entre os orógenos Araçuaí e Ribeira. In: Dissertação de Mestrado, Instituto de Geociências, Universidade Federal de Minas Gerais, p. 104.
Frimmel, H., Frank, W., 1998. Neoproterozoic tectono-thermal evolution of the Gariep Belt and its basement, Namibia and South Africa. Precambrian Res. 90, 1–28, http://dx.doi.org/10.1016/S0301-9268(98)00029-1.
Gonçalves, L., Alkmim, F.F., Pedrosa-Soares, A.C., Dussin, I.A., Valeriano, C.M., 2015. Granites of the intracontinental termination of a magmatic arc: an example from the Ediacaran Araçuaí orogen, southeastern Brazil. Gondwana Res., http://dx.doi.org/10.1016/j.gr.2015.07.015, http://dx.doi.org/10.1016/j.gr.2015.07.015.
Gonçalves, L., Farina, F., Lana, C., Pedrosa-Soares, A.C., Alkmim, F., Nalini Jr., H.A., 2014. New U–Pb ages and lithochemical attributes of the Ediacaran Rio Doce magmatic arc, Araçuaí confined orogen, southeastern Brazil. J. S. Am. Earth Sci. 52, 129–148.
Goscombe, B., Gray, D., Armstrong, R., Foster, D.A., Vogl, J., 2005. Event geochronology of the Pan-African Kaoko Belt, Namibia. Precambrian Res. 140, 103.e1–103.e41.
Gradim, C.T., 2013. Complexo Nova Venécia e Magmatismo Associado, Orógeno Araçuaí, Estado do Espírito Santo, MS Dissertation. Universidade Federal de Minas Gerais, Belo Horizonte, pp. 96.
Gradim, C., Roncato, J., Pedrosa-Soares, A.C., Cordani, U., Dussin, I., Alkmim, F.F., Queiroga, G., Jacobsohn, T., Silva, L.C., da Babinski, M., 2014. The hot back-arc zone of the Araçuaí orogen, Eastern Brazil: from sedimentation to granite generation. Braz. J. Geol. 44, 155–180, http://dx.doi.org/10.5327/Z2317-4889201400010012.
Gray, D.R., Foster, D.A., Meert, J.G., Goscombe, B.D., Armstrong, R., Trouw, R.A.J., Passchier, C.W., 2008. A Damara orogen perspective on the assembly of southwestern Gondwana. Geol. Soc. Lond., http://dx.doi.org/10.1144/SP294.14.
Heilbron, M., Machado, N., 2003. Timing of terrane accretion in the Neoproterozoic-Eopaleozoic Ribeira Orogen (se Brazil). Precambrian Res. 125, 87–112, http://dx.doi.org/10.1016/S0301-9268(03)00082-2.
Heilbron, M., Tupinambá, M., Valeriano, C.D.M., Armstrong, R., Do Eirado Siva, L.G., Melo, R.S., Simonetti, A., Pedrosa Soares, A.C., Machado, N., 2013. The Serra da Bolívia complex: the record of a new Neoproterozoic arc-related unit at Ribeira belt. Precambrian Res. 238, 158–175, http://dx.doi.org/10.1016/j.precamres.2013.09.014.
Holland, T., Powell, R., 2003. Activity-composition relations for phases in petrological calculations: an asymmetric multicomponent formulation. Contrib. Mineral. Pet. 145, 492–501.
Holland, T.J.B., Powell, R., 1998. An internally consistent thermodynamic data set for phases of petrological interest. J. Metamorph. Geol. 16, 309–343, http://dx.doi.org/10.1111/j.1525-1314.1998.00140.x.
Jung, S., Mezger, K., 2003. Petrology of basement-dominated terranes: I. Regional metamorphic T-t path from U–Pb monazite and Sm-Nd garnet geochronology (Central Damara orogen, Namibia). Chem. Geol. 198, 223–247, http://dx.doi.org/10.1016/S0009-2541(03)00037-8.
Korhonen, F.J., Brown, M., Grove, M., Siddoway, C.S., Baxter, E.F., Inglis, J.D., 2012. Separating metamorphic events in the Fosdick migmatite-granite complex, West Antarctica. J. Metamorph. Geol. 30, 165–192, http://dx.doi.org/10.1111/j.1525-1314.2011.00961.x.
Ludwig, K.R., 2003. Using Isoplot/Ex, version 3.00, a Geochronological Toolkit for Microsoft Excel, Special Publication 1. Berkeley Geochronology Center, pp. 43.
Mendes, J.C., de Medeiros, S.R., McReath, I., de Campos, C.M.P., 2005. Cambro-Ordovician magmatism in SE Brazil: U–Pb and Rb-Sr ages, combined with Sr and Nd isotopic data of Charnockitic rocks from the Varzea Alegre Complex. Gondwana Res. 8, 337–345, http://dx.doi.org/10.1016/S1342-937X(05)71139-4.
Montel, J.M., Vielzeuf, D., 1997. Partial melting of metagreywackes. Part II. Compositions of minerals and melts. Contrib. Mineral. Petrol. 128, 176–196, http://dx.doi.org/10.1007/s004100050302.
Munhá, J.M.U., Cordani, U.G., Tassinari, C.C.G., Palácios, T., 2005. Petrologia e termocronologia de gnaisses migmatíticos da Faixa de Dobramentos Araçuaí (Espírito Santo, Brasil). Rev. Bras. Geociênc. 35 (1), 123–134.
Nalini Jr., H.A., Bilal, E., Correia-Neves, J.M., 2000. Syncollisional peraluminous magmatism in the Rio Doce region: mineralogy, geochemistry and isotopic data of the Urucum suite (eastern Minas Gerais state, Brazil). Rev. Bras. Geociênc. 30 (1), 120–125.
Nalini Jr., H.A., 1997. Caracterisation des suites magmatiques néoproterozoïques de la region de Conselheiro Pena et Galiléia (Minas Gerais, Bresil). Etude geochimique et structural des suites Galiléia et Urucum et relation avec les pegmatites a élements rares associées. These de doctoral. In: Ecole Nationale Superieure de Mines de Paris et de Saint Etienne, p. 237.
Nicoli, G., Stevens, G., Moyen, J.-F., Frei, D., 2014. Rapid evolution from sediment to anatectic granulite in an Archean continental collision zone: the example of the Bandelierkop Formation metapelites, South Marginal Zone, Limpopo Belt, South Africa. J. Metamorph. Geol. 33, 177–202, http://dx.doi.org/10.1111/jmg.12116.
Noce, C.M., Pedrosa-Soares, A.C., Piuzana, D., Armstrong, R., Laux, J.H., Campos, C.M., Medeiros, S.R., 2004. Ages of sedimentation of the kinzigitic complex and of a late orogenic thermal episode in the Araçuaí orogen, Northern Espírito Santo State, Brazil: Zircon and monazite U–Pb SHRIMP and ID-TIMS data. Rev. Bras. Geociênc. 34, 587–592.
Noce, C.M., Teixeira, W., Quéméneur, J.J.G., Martins, V.T.S., Bolzachini, É., 2000. Isotopic signatures of Paleoproterozoic granitoids from the southern Sao Francisco Craton and implications for the evolution of the Transamazonian Orogeny. J. South Am. Earth Sci. 13, 225–239, http://dx.doi.org/10.1016/S0895-9811(00)00019-5.
Novo, T.A., 2013. Caracterização do Complexo Pocrane, magmatismo básico mesoproterozóico e unidades neoproterozóicas do sistema Araçuaí-Ribeira, com ênfase em geocronologia U–Pb (SHRIMP e LA-ICP-MS). Universidade Federal de Minas Gerais, Belo Horizonte, pp. 193.
Novo, T.A., Pedrosa-Soares, A.C., Noce, C.M., Alkmim, F.F., Dussin, I., 2010. Rochas charnockíticas do sudeste de Minas Gerais: a raiz granulítica do arco magmático do Orógeno Araçuaí. Rev. Bras. Geociênc. 40, 573–592.
Paes, V.J.C., 1999. Geologia e geoquímica de rochas metamáficas e meta-ultramáficas da região de Alvarenga-MG e suas implicações geotectônicas. Instituto de Geociências, Universidade Federal de Minas Gerais, Belo Horiz., pp. 153, Dissertação de Mestrado.
Paes, V., Raposo, F., Pinto, C.P., Oliveira, F., 2010. Projeto Jequitinhonha, Estados de Minas Gerais e Bahia: texto explicativo. Geologia e Recursos Minerais das Folhas Comercinho, Jequitinhonha, Almenara, Itaobim, Joaíma e Rio do Prado. CPRM, Belo Horizonte, pp. 376.
Patiño Douce, A.E., Johnston, A.D., 1991. Phase equilibria and melt productivity in the pelitic system: implications for the origin of peraluminous granitoids and aluminous granulites. Contrib. Mineral. Petrol. 107, 202–218, http://dx.doi.org/10.1007/BF00310707.
Pedrosa-Soares, A.C., Noce, C.M., Wiedemann, C., Pinto, C.P., 2001. The Araçuaí-West-Congo Orogen in Brazil: Na overview of a confined orogen formed during Gondwanalandassembly. Precambrian Res. 110, 307–323.
Pedrosa-Soares, A.C., Alkmim, F.F., 2011. How many rifting events preceded the development of the Araçuaí – West Congo orogen? Geonomos 19, 244–251.
Pedrosa-Soares, A.C., Alkmim, F.F., Tack, L., Noce, C.M., Babinski, M., Silva, L.C., Martins-Neto, M.A., 2008. Similarities and differences between the Brazilian and African counterparts of the Neoproterozoic Aracuai-West Congo orogen. Geol. Soc. Lond. Spec. Publ.
Pedrosa-Soares, A.C., De Campos, C.P., Noce, C., Silva, L.C., Novo, T., Roncato, J., Medeiros, S., Castaneda, C., Queiroga, G., Dantas, E., Dussin, I., Alkmim, F., 2011. Late Neoproterozoic-Cambrian granitic magmatism in the Aracuai orogen (Brazil), the Eastern Brazilian Pegmatite Province and related mineral resources. Geol. Soc. London, Spec. Publ.
Pedrosa-Soares, A.C., Noce, C.M., Alkmim, F.F., Silva, L.C.S., Babinski, M., Cordani, U., Castañeda, C., 2007. Orógeno araçuaí: síntese do conhecimento 30 anos após almeida 1977. Geonomos 15, 1–16.
Pedrosa-Soares, A.C., Castañeda, C., Queiroga, G., Gradim, C., Belém, J., Roncato, J., Novo, T., Dias, P., Gradim, D., Medeiros, S., Jacobsohn, T., Vieira, V., 2006. Magmatismo e tectônica do Orógeno Araçuaí na região entre 18° – 19° S e 41° – 40° 30' W, extremo leste de Minas e norte do Espírito Santo. Geonomos 14 (1–2), 97–111.
Peixoto, E., Pedrosa-Soares, A.C., Alkmim, F.F., Dussin, I.A., 2014. A suture-related accretionary wedge formed in the Neoproterozoic Araçuaí Orogen (SE Brazil) during Western Gondwanaland assembly. Gondwana Res., http://dx.doi.org/10.1016/j.gr.2013.11.010.
Petitgirard, S., Vauchez, A., Egydio-Silva, M., Bruguier, O., Camps, P., Monié, P., Babinski, M., Mondou, M., 2009. Conflicting structural and geochronological data from the Ibituruna quartz-syenite (SE Brazil): effect of protracted "hot" orogeny and slow cooling rate? Tectonophysics 477, 174–196.
Pickering, J.M., Johnston, D.A., 1998. Fluid-absent melting behavior of a two-mica metapelite: experimental constraints on the origin of black hills granite. J. Petrol. 39, 1787–1804, http://dx.doi.org/10.1093/petroj/39.10.1787.
Porada, H., 1989. Pan-African rifting and orogenesis in southern to equatorial Africa and eastern Brazil. Precambrian Res., http://dx.doi.org/10.1016/0301-9268(89)90078-8.
Pullen, A., Ibáñez-Mejía, M., Gehrels, G.E., Ibáñez-Mejía, J.C., Pecha, M., 2014. What happens when $n = 1000$? Creating large-n geochronological datasets with LA-ICP-MS for geologic investigations. J. Anal. At. Spectrom. 29, 971, http://dx.doi.org/10.1039/c4ja00024b.
Queiroga, G.N., Pedrosa-Soares, A.C., Noce, C.M., Alkmim, F.F., Pimentel, M.M., Dantas, E., Martins, M., Castañeda, C., Suita, M.T.F., Prichard, F., 2007. Age of the Ribeirão da Folha ophiolite, Araçuaí Orogen: The U–Pb zircon dating of a plagiogranite. Geonomos 15, 61–65.
Richter, F., 2015. Sedimentation, metamorphism and granite generation in a back-arc region: the crustal processes recorded in the Ediacaran Nova Venécia Complex (Araçuai Orogen, Southeas Brazil), MSc dissertation, Universidade Federal de Ouro Preto. Contribuições as Ciências da Terra, Série M 74 (326), 160.
Rogers, J.J.W., Santosh, M., 2004. Continents and Supercontinents. Oxford University Press, Oxford.
Roncato, J.G., 2009. As suítes graníticas tipo-S do norte do Espírito Santo na região das folhas Ecoporanga, Mantena, Montanha e Nova Venécia, MSc Dissertation. Universidade Federal de Minas Gerais, Belo Horizonte, pp. 102.

Rosa, M.d.L.d.S., Conceição, H., Macambira, M.J.B., Galarza, M.A., Cunha, M.P., Menezes, R.C.L., Marinho, M.M., Filho, B.E.d.C., Rios, D.C., 2007. Neoproterozoic anorogenic magmatism in the Southern Bahia Alkaline Province of NE Brazil: U–Pb and Pb-Pb ages of the blue sodalite syenites. Lithos 97, 88–97.

Royden, L., 1996. Coupling and decoupling of crust and mantle in convergent orogens: implications for strain partitioning in the crust. J. Geophys. Res. 101, http://dx.doi.org/10.1029/96JB00951.

Sawyer, E.W., 371 pp. 2008. Atlas of Migmatites. The Canadian Mineralogist, Special Publication 9. NRC Research Press, Ottawa, Ontario, Canada.

Schmitt, R.S., Trouw, R.A.J., Van Schmus, W.R., Pimentel, M.M., 2004. Late amalgamation in the central part of Western Gondwana: new geochronological data and the characterization of a Cambrian collision orogeny in the Ribeira Belt (SE Brazil). Precambrian Res. 133, 29–61.

Silva, L.C., da Pedrosa-Soares, A.C., Armstrong, R., Noce, C.M., 2011. Determinando a duração do período colisional do Orógeno Araçuaí com base em geocronologia U–Pb de alta resolução em zircão: uma contribuição para a história da amalgamação do Gondwana Ocidental. Geonomos 19, 180–197.

Silva, L.C., da Pinto, C.P., Gomes, A.C., Paes, V.C., Chemale, F., 2007. Granitogenesis at the northern tip of the Araçuaí Orogen, SE Brazil: LA-ICP-MS U–Pb zircon geochronology, and tectonic significance. In: Simpósio de Geologia do Sudeste. Diamantina, Anais, pp. 20–21.

Silva, L.C., da Armstrong, R., Delgado, I.M., Pimentel, M., Arcanjo, J.B., Melo, R.C., Teixeira, L., Jost, H., Cardoso Filho, J.M., Pereira, L.H.M., 2002. Reavaliação da evolução geológica em terrenos pré- cambrianos brasileiros com base em novos dados U=Pb SHRIMP, parte I: limite centro-oriental do cráton são francisco na bahia(*). Rev. Bras. Geociênc. 32, 501–512.

Silva, L.C., da McNaughton, N.J., Armstrong, R., Hartmann, L.A., Fletcher, I.R., 2005a. The neoproterozoic Mantiqueira Province and its African connections: a zircon-based U–Pb geochronologic subdivision for the Brasiliano/Pan-African systems of orogens. Precambrian Res. 136, 203–240.

Silva, L.C., da McNaughton, N.J., Fletcher, I.R., 2005b. SHRIMP U–Pb zircon geochronology of Neoproterozoic crustal granitoids (Southern Brazil): a case for discrimination of emplacement and inherited ages. Lithos 82, 503–525, http://dx.doi.org/10.1016/j.lithos.2004.09.029.

Silva, L.C., da Pedrosa-Soares, A.C., Teixeira, L.R., Armstrong, R., 2008. Tonian rift-related, A-type continental plutonism in the Araçuaí Orogen, eastern Brazil: new evidence for the breakup stage of the São Francisco-Congo Paleocontinent. Gondwana Res. 13, 527–537, http://dx.doi.org/10.1016/j.gr.2007.06.002.

Sircombe, K.N., 2006. Mountains in the shadows of time: Three-dimensional density distribution mapping of U-Pb isotopic data as a visualization aid for geochronological information in concordia diagrams. Geochem. Geophys. Geosyst. 7, Q07013, http://dx.doi.org/10.1029/2005GC001052.

Söllner, F., Lammerer, B., Weber-Diefenbach, K., 1991. Die Krustenentwicklung in Der Küstenregion Nördlich Von Rio de Janeiro, Brasilien. Münchener Geowissenschaftliche Hefte 11. Friedrich Pfeil Verlag, München, pp. 4.

Stevens, G., Gibson, R.L., Droop, G.T.R., 1997. Mid-crustal granulite facies metamorphism in the Central Kaapvaal craton: the Bushveld Complex connection. Precambrian Res., http://dx.doi.org/10.1016/S0301-9268(96)00043-5.

Stevens, G., van Reenen, D., 1992. Constraints on the form of the P-T loop in the Southern Marginal Zone of the Limpopo Belt, South Africa. Precambrian Res., http://dx.doi.org/10.1016/0301-9268(92)90028-M.

Taylor, J., Nicoli, G., Stevens, G., Frei, D., Moyen, J.F., 2014. The processes that control leucosome compositions in metasedimentary granulites: perspectives from the Southern Marginal Zone migmatites, Limpopo Belt, South Africa. J. Metamorph. Geol. 32, 713–742, http://dx.doi.org/10.1111/jmg.12087.

Trouw, R., Heilbron, M., Ribeiro, A., Paciullo, F., Valeriano, C.M., Almeida, J.C.H., Tupinambá, M., Andreis, R.R., 2000. The central segment of the Ribeira Belt. In: Cordani, UG, Milani, EJ, Thomaz Filho, A, Campos, DA (Eds.), Tectonic Evolution of South America. , pp. 287–310, Rio de Janeiro.

Tupinambá, M., Heilbron, M., Valeriano, C., Júnior, R.P., de Dios, F.B., Machado, N., Silva, L.G.d.E., de Almeida, J.C.H., 2012. Juvenile contribution of the Neoproterozoic Rio Negro Magmatic Arc (Ribeira Belt, Brazil): implications for Western Gondwana amalgamation. Gondwana Res. 21, 422–438, http://dx.doi.org/10.1016/j.gr.2011.05.012.

Valeriano, C., Pimentel, M., 2008. Tectonic evolution of the Brasília Belt, Central Brazil, and early assembly of Gondwana. Geol. Soc. 294, 197–210, http://dx.doi.org/10.1144/SP294.11.

Vanderhaeghe, O., Teyssier, C., 2001. Partial melting and flow of orogens. Tectonophysics 342, 451–472, http://dx.doi.org/10.1016/S0040-1951(01) 00175-5.

Vauchez, A., Egydio-Silva, M., Babinski, M., Tommasi, A., Uhlein, A., Liu, D., 2007. Deformation of a pervasively molten middle crust: Insights from the neoproterozoic Ribeira-Araçuaí orogen (SE Brazil). Terra Nov. 19, 278–286, http://dx.doi.org/10.1111/j.1365-3121.2007.00747.x.

Vernon, R.H., 2011. Microstructures of melt-bearing regional metamorphic rocks. GSA Mem. 207, 1–11, http://dx.doi.org/10.1130/2011.1207(01).

Vielzeuf, D., Holloway, J.R., 1988. Experimental determination of the fluid-absent melting relations in the pelitic system – consequences for crustal differentiation. Contrib. Mineral. Petrol. 98, 257–276, http://dx.doi.org/10.1007/BF00375178.

White, R.W., Pomroy, N.E., Powell, R., 2005. An in situ metatexite-diatexite transition in upper amphibolite facies rocks from Broken Hill, Australia. J. Metamorph. Geol. 23, 579–602.

White, R.W., Powell, R., 2002. Melt loss and the preservation of granulite facies mineral assemblages. J. Metamorph. Geol. 20, 621–632, http://dx.doi.org/10.1046/j.1525-1314.2002.00206.x.

White, R.W., Powell, R., Clarke, G.L., 2002. The interpretation of reaction textures in Fe-rich metapelite granulites of the Musgrave Block, central Australia: constraints from mineral equilibria calculations in the system K_2O–FeO–MgO–Al_2O_3–SiO_2–H_2O–TiO_2–Fe_2O_3. J. Metamorph. Geol. 20, 41.

White, R.W., Powell, R., Holland, T.J.B., Worley, B.A., 2000. The effect of TiO_2 and Fe_2O_3 on metapelitic assemblages at greenschist and amphibolite facies conditions: mineral equilibria calculations in the system K2O-FeO-MgO-Al2O3-SiO2-H2O-TiO2-Fe2O3. J. Metamorph. Geol. 18, 497–511.

White, R.W., Powell, R., Holland, T.J.B., 2007. Progress relating to calculation of partial melting equilibria for metapelites. J. Metamorph. Geol. 25, 511–527, http://dx.doi.org/10.1111/j.1525-1314.2007.00711.x.

Whittington, A.G., Connelly, J., Pedrosa-Soares, A.C., Marshak, S., Alkmim, F.F., 2001. Collapse and melting in a confined orogenic belt: Preliminary results from the Neoproterozoic Araçuaí belt of eastern Brazil. In: American Geophysical Union Meeting, San Francisco, pp. p.1181–p.1182, Abstract T32B-0895, v. 82.